Single-Cell Transcriptomics Reveals Dynamic Microglial States and Neural-Immune Networks in Human Diabetic Retinopathy

Luning Yang[1], Sen Lin[1], Yiwen Tao[1], Qi Pan[1], Tengda Cai[1], Yunyan Ye[2], Jianhui Liu[3], Yang Zhou[4], Quanyong Yi[5], Zen Haut Lu[6], Lie Chen[6], Gareth McKay[7], Richard Rankin[8], Yongqing Shao[5*], Weihua Meng[1,9,10*]

1 Nottingham Ningbo China Beacons of Excellence Research and Innovation Institute, University of Nottingham Ningbo China, Ningbo, China, 315100

2 Department of Ophthalmology, Lihuili Hospital affiliated with Ningbo University, Ningbo, China, 315040

3 Department of Cardiology, Lihuili Hospital affiliated with Ningbo University, Ningbo, China, 315040

4 Ningbo Institute of Innovation for Combined Medicine and Engineering, The Affiliated Li Huili Hospital, Ningbo University, Ningbo, China, 315201

5 Department of Ophthalmology, The Affiliated Ningbo Eye Hospital of Wenzhou Medical University, Ningbo, China, 315040

6 PAPRSB Institute of Health Sciences, Universiti Brunei Darussalam, Bandar Seri, Begawan, Brunei Darussalam, BE1410

7 Centre for Public Health, Institute of Clinical Science, Queen's University Belfast, Block B, Royal Hospital, Grosvenor Road, Belfast, UK, BT12 6BA

8 School of Mathematical Sciences, University of Nottingham Ningbo China, Ningbo, China, 315100

9 Division of Population Health and Genomics, School of Medicine, University of Dundee, Dundee, UK, DD2 4BF

10 Center for Public Health, Faculty of Medicine, Health and Life Sciences, School of Medicine, Dentistry and Biomedical Sciences, Queen's University Belfast, Belfast, UK, BT12 6BA

Corresponding Author:

Dr Weihua Meng

Address: Nottingham Ningbo China Beacons of Excellence Research and Innovation Institute, University of Nottingham Ningbo China, Ningbo, China, 315100. Tel: +86 574 88188632. Email: weihua.meng@nottingham.edu.cn. ORCID: 0000-0001-5388-8494

Dr Yongqing Shao

Address: Department of Ophthalmology, The Affiliated Ningbo Eye Hospital of Wenzhou Medical University, Ningbo, China, 315040. Tel: +86 15968412426. Email: sunniesyq@163.com. ORCID: 0009-0006-1319-8521

ORCID codes

Luning Yang: 0000-0001-9056-5950

Sen Lin: 0000-0002-7695-0964

Yiwen Tao: 0009-0000-0102-4205

Qi Pan: 0000-0003-0135-9122

Tengda Cai: 0000-0003-1617-506X

Yunyan Ye: 0009-0005-2325-1405

Jianhui Liu: 0009-0004-1341-0831

Yang Zhou: 0000-0001-9273-0489

Quanyong Yi: 0000-0002-9369-3998

Zen Haut Lu: 0000-0002-9408-0579

Lie Chen: 0000-0001-9764-4299

Gareth McKay: 0000-0001-8197-6280

Richard Rankin: 0000-0001-6445-2602

Yongqing Shao: 0009-0006-1319-8521

Weihua Meng: 0000-0001-5388-8494

Abstract

Diabetic retinopathy (DR) is a major cause of vision loss worldwide. Here, we perform single-cell RNA sequencing of thirteen human retina samples (from living and post-mortem donors) across non-diabetic, diabetic, and DR states to create a comprehensive transcriptomic atlas. We uncover three distinct microglial states—homeostatic, stress-response, and inflammatory—along a functional continuum, rather than discrete activation states, with dynamic transitions occurring throughout disease progression. Trajectory analysis indicates bifurcating paths starting from the homeostatic state branching toward stress-response and inflammatory states. Three major functional modules: ribosomal/translation, coordinated immune cell function, and inflammatory/transcriptional regulation, showing disease-specific activation patterns were identified. Cell communication analysis further highlights sophisticated neural-immune interactions, particularly between photoreceptors and microglia. Our findings provide insights into the complex cellular dynamics of DR progression and suggest potential therapeutic targets for early intervention.

Keywords: Single-cell RNA sequencing; Human retina: diabetic retinopathy; Microglial states; Neural-immune interactions; diabetes

Introduction

Diabetic retinopathy (DR) is the leading cause of vision impairment and blindness among working-age adults globally, posing a significant public health issue. It is characterized by progressive neurovascular dysfunction, involving both neurodegeneration and microvascular changes [1]. The global number of adults with diabetes has surpassed 800 million, and the global prevalence of diabetes in adults has risen from 7% to 14% [2]. Among those with diabetes, 22.27% are affected by DR, and from 1990 to 2020, the global age-standardized prevalence of blindness caused by diabetic eye disease increased by 14.9%, reaching 18.5% [3]. This trend poses a significant and growing burden on global health. While significant progress has been made in the treatment of DR, substantial limitations remain. Anti-VEGF therapy, panretinal photocoagulation, and corticosteroid treatments have demonstrated efficacy, but they are associated with incomplete responses, visual side effects, and complications [4, 5]. These therapies primarily target downstream effects rather than addressing the underlying pathogenic mechanisms [6].

The key gap in DR treatment lies in the focus on late-stage manifestations, with insufficient intervention in early molecular events, failing to address the complex cellular and molecular mechanisms underlying disease progression [7]. Therefore, a comprehensive understanding of pathophysiology is needed, particularly to intervene in the early stages when the disease is most controllable. Targeted treatment at the cellular level, rather than addressing downstream complications, is crucial. This requires a deeper understanding of single-cell and molecular mechanisms [8].

While single-cell RNA sequencing (scRNA-seq) has emerged as a powerful tool for understanding complex biological systems, its application in DR research faces several critical limitations. The major challenge in the application of scRNA-seq in DR research is the difficulty in obtaining human retina DR samples. While a few single-cell transcriptomic studies have generated retinal atlases, most published

datasets utilize healthy donor eyes rather than samples from specific disease conditions, limiting our understanding of pathological states. To date, while several studies have examined retinal transcriptomes in animal models or healthy human retinas, comprehensive single-cell analysis of complete human DR retina samples remains notably absent. Two recent studies focused on fibrovascular membranes, surgically harvested vitreous and peripheral blood from proliferative diabetic retinopathy (PDR) patients [9, 10], but neither fully recapitulates the complete pathogenesis of human DR as they focused on specific tissue types rather than the retina. Another challenge is the rapid post-mortem degradation of retinal tissue. In addition, the high cost of scRNA-seq and the difficulty in obtaining human retinal tissues hinder its large-scale application in DR and phased experimental design.

To investigate DR in retinal samples, more and more recent studies have focused on microglial cells, as these resident tissue macrophages play a pivotal role in initiating and exacerbating retinal inflammatory responses [11]. However, two significant challenges have emerged in current DR research. First, the detection of microglia clusters in non-DR samples is challenging due to their rapid environmental responsiveness [12], particularly in post-mortem specimens. The second challenge lies in distinguishing DR-specific microglial responses from general retinal inflammation. Microglia undergo activation in multiple retinal pathologies, including age-related macular degeneration, glaucoma, and retinitis pigmentosa [13, 14]. While microglial activation is a hallmark of DR, these cells also become activated in various retinal pathologies [15], making it difficult to identify DR-specific signatures. In all these conditions, activated microglia share common features such as increased proliferation, migration to sites of damage, and production of pro-inflammatory mediators, regardless of the underlying disease mechanism. This widespread activation across different eye conditions makes it challenging to identify DR-specific signatures. Our study addresses these fundamental limitations through innovative

approaches. We utilized thirteen fresh human retinal samples, collected from both living donors and post-mortem specimens with minimal processing time, maximizing transcriptional fidelity. Moreover, the fresh retinal samples from living donors mostly keep the general inflammatory profiles compared to post-mortem samples. We employed an integrated analytical approach to comprehensively characterize the cellular and molecular features of DR progression using these samples (Figure 1).

Our integrated analysis reveals three critical insights that address fundamental gaps in the field. First, we demonstrate that retinal microglia exist along a functional continuum rather than discrete activation states during DR progression, with three distinct states showing dynamic shifts in their relative proportions. Second, we uncover previously unrecognized communication networks between multiple retinal cell types, particularly through the MIF-CD74-CXCR4 signaling axis. Third, we identify distinct rod states with unique molecular signatures and adaptation mechanisms. This study represents the first comprehensive single-cell analysis of human DR progression, uncovering a sophisticated interplay between neural and immune responses. These findings could advance our understanding of DR pathogenesis and open new avenues for targeted therapeutic interventions.

Materials and Methods

Human donor eyes collections for scRNA-seq analysis

From June 2023 to July 2024, we obtained thirteen human retina samples under protocols approved by the ethics committees of the University of Nottingham Ningbo China, the Lihuili Hospital, and the Ningbo Eye Hospital. Two samples were acquired through surgical enucleation at the Lihuili Hospital with patient consent. The remaining eleven samples came from the Ningbo Eye Hospital, comprising four paired eyes from deceased donors and three surgical specimens from enucleation procedures. We

137 utilized complete retinal specimens rather than selective punch biopsies, enabling comprehensive
138 analysis of the entire retinal structure from center to periphery. In this study, 'fresh retinal samples' refers
139 to two categories, the first is the living donor samples obtained during surgical enucleation and processed
140 immediately within 10 minutes, and the second is post-mortem specimens processed within 12 hours of
141 death with strict temperature control without freezing. Supplementary Table S1 provides detailed
142 information on each sample.
143
144 **Single-cell RNA sequencing**
145 Human retina samples were dissociated for scRNA-seq using the LK003150-1bx Dissociation Kit
146 (Worthington Biochemical Corporation) following the manufacturer's protocol. Tissue was placed on ice
147 in a petri dish and manually cut into 2–4 mm pieces. After incubation in RPMI/enzyme mix (Miltenyi
148 Biotec), the tissue fragments were transferred to a gentleMACS C tube for dissociation. After dissociation,
149 the suspension was passed through a 70 μm cell strainer and centrifuged at 300 × g for 10 minutes at
150 4°C. The supernatant was removed, and 10 volumes of 1x Red Blood Cell Lysis Solution (130-094-183,
151 Miltenyi Biotec) were added to lyse red blood cells at 4°C for 10 minutes. Subsequently, 10 mL of 1x
152 PBS containing 0.04% BSA was added to the suspension, which was then centrifuged again at 300 × g
153 for 10 minutes. The suspension was mixed with AO/PI fluorescent dye (1:1 ratio) and incubated for 30
154 seconds, then cell viability was assessed for CountStar analysis. Viable cell suspension was resuspended
155 in 1x PBS with 0.04% BSA to 700-1200 cells/μL (viability > 85%) for loading onto the 10x Genomics
156 Chromium platform.
157 scRNA-seq libraries were made from 10,000 cells per sample using the Chromium Single Cell 3' Library
158 and Gel Bead Kit (10X Genomics). Raw BCL files were converted to FASTQ files using Illumina's

bcl2fastq converter after library preparation. Three criteria were checked as the main quality control of the raw data: no more than three "N" bases; no more than 20% of bases had a quality score lower than 5; and adapter sequence detection. The resulting sequencing outputs were processed using the 10X Genomics Cell Ranger V8.0.1 pipeline with default settings. Transcript reads were quantified using the 10x Genomics Human reference index (GRCh38-2020-A). Each cell was assigned a unique, sample-specific identifier, and feature-barcode matrices were generated using the chromium cellular barcodes.

Quality control and doublets removal

For each sample, feature-barcode matrices were processed using the 10X Genomics Cell Ranger pipeline (https://support.10xgenomics.com/single-cell-gene-expression/software/pipelines/latest/what-is-cell-ranger). We performed quality control and doublet removal separately for each dataset to eliminate low-quality cells. Doublets were identified and removed using DoubletFinder (https://github.com/chris-mcginnis-ucsf/DoubletFinder). High-quality cells were selected based on the following criteria in the Seurat R package (v5.1.0) [16]: cells with a minimum gene count of 200, a UMI count greater than 400, and a mitochondrial read fraction of less than 20%. Cells passing these filters were retained for downstream analysis.

Data integration and clustering

After initial processing, the thirteen datasets were integrated by scanpy (v1.10.2) [17]. We used scvi-tools (v1.1.2) [18] to perform dimensionality reduction and batch-effect correction. A k-nearest neighbor (KNN) graph was built from the resulting latent space, and Leiden clustering was applied at multiple resolutions to identify and refine retinal cell types. The marker gene expression of each cluster was used

181 to annotate their corresponding retina cell type. This annotation workflow was further repeated to refine
182 an accurate cell type annotation for the sub populations within each cell type. Sample bias introduced by
183 the inclusion of fresh retinas from living donors was evaluated by analyzing the proportions of various
184 cell types across all datasets. To ensure data quality and technical consistency, three samples (Sample 1,
185 10, and 11) with unusually low rod proportions (38-51% compared to the typical range of 70-82%
186 observed in other samples) were excluded from downstream analyses of microglia, as shown in
187 Supplementary Table S1. This quality control step was performed prior to any disease-specific analyses
188 to prevent technical artifacts from confounding biological interpretations.
189

190 **Cell abundance and disturbance analysis**

191 Transcriptomic variations across nonDM (samples without diabetes), DM (samples with diabetes), and
192 DR (samples with diabetic retinopathy) conditions were assessed using scDist (v1.1.2) [19], Augur
193 (v1.0.3) [20], and miloR (v1.10.0) [21]. scDist quantified the three disease states impacts on retinal cell
194 types while accounting for random effects by unique sample identifiers. Augur calculated the Area Under
195 the Curve (AUC) scores to evaluate the predictive power of gene expression profiles and miloR assessed
196 differential cell population abundances. For both Augur and miloR analyses, we focused on comparing
197 nonDM and DR conditions because these tools are designed for pairwise comparisons and do not support
198 simultaneous analysis of multiple conditions. Moreover, comparing nonDM and DR conditions captures
199 the significant disease profiles, as significant transcriptomic changes are more pronounced in DR
200 compared to the subtle, inconsistent alterations observed in DM stage.
201

202 **Differential expression and enrichment analysis**

We performed differential expression (DE) to identify cell type or condition-specific markers using Seurat's FindAllMarkers and FindMarkers functions with an FDR < 0.05 and |log2FC| > 1 threshold for significance. Gene Ontology (GO) enrichment analysis was conducted by clusterProfiler (v4.10.1) [22]. Pathway scoring and enrichment were further evaluated by the irGSEA (v3.3.2) [23] framework, combining multiple methods (AUCell, UCell, singscore, ssgsea, JASMINE, viper) through robust rank aggregation (RRA).

Transcriptional pattern discovery

Microglia-specific gene co-expression modules were identified using three complementary approaches. First, Hotspot analysis (v1.1.1) identified spatially coordinated gene modules based on local correlation (https://github.com/YosefLab/Hotspot), leveraging dimensionality reduction and KNN graph construction. Second, CoGAPS analysis (v3.25.2) applied Bayesian non-negative matrix factorization to reveal key transcriptional patterns and associated marker genes (https://github.com/FertigLab/CoGAPS). Pattern marker genes were identified followed by MSigDB Hallmark enrichment analysis. Finally, hdWGCNA analysis (v0.3.03) identified co-expressed gene modules through weighted correlation network analysis [24]. Module relationships were evaluated through correlation analysis, with scores calculated using UCell (v2.6.2) [25]. Expression patterns were compared across disease conditions using violin plots and t-tests. GO enrichment analysis was performed using clusterProfiler.

Developmental trajectory analysis

Microglial developmental trajectories and gene expression dynamics were analyzed using complementary approaches. CytoTRACE2 (v1.0.0) assessed differentiation potential based on

transcriptional diversity across integrated and condition-specific datasets (DR and nonDM) [26]. For trajectory reconstruction, we utilized monocle2 (v2.32.0) and monocle3 (v1.3.7) to examine pseudotime dynamics [27], identifying key genes and transitions during disease progression. To integrate trajectory and transcriptional analyses, we examined the temporal dynamics of Hotspot modules along the monocle3 pseudotime trajectory. Cells were binned into discrete pseudotime intervals, and module scores were calculated for each Hotspot module (M1-M7) using AddModuleScore function. Module activities were analyzed separately for DR and nonDM conditions to examine disease-specific variations along their respective trajectories. Finally, RNA velocity analysis was performed using dynamo (v1.4.0) to predict transcriptional dynamics and cell state transitions [28]. Velocyto (v0.17.17) was first applied to generate spliced and unspliced expression matrices from Cell Ranger output files for each sample [29].

Transcriptional regulatory network analysis

To analyze transcriptional regulatory networks, we employed two complementary approaches. SCENIC (v1.1.2.2) identified transcription factor (TF) target relationships using GRNBoost2 algorithm with sparse optimization [30]. Subsequent cisTarget analysis used hg38 motif rankings database for hg38 (10kb up/downstream of TSS) with clustered motif collection v10, obtained from the Aerts lab resources (https://resources.aertslab.org/cistarget/). For each condition (nonDM, DM, DR), regulon specificity scores (RSS) were calculated with results visualized using Z-score normalized heatmaps. We also performed connection specificity index (CSI) analysis to identify co-regulated TF pairs, followed by hierarchical clustering that grouped them into distinct modules.

Cell communication analysis

247 CellChat (v1.6.1) was applied to perform cell-cell communication analysis [31]. First, CellChat objects
248 were created for DR and nonDM conditions using the human CellChatDB database. Overexpressed genes
249 and interactions were identified with default parameters and the analysis was enhanced by projecting
250 data onto protein-protein interaction networks. Communication probabilities were computed using the
251 triMean method. Signaling pathway analysis was performed by aggregating the communication
252 probabilities of all ligand-receptor pairs associated with each pathway. For comparison between
253 conditions, we examined both source and target relationships of microglia subtypes (Microglia_1,
254 Microglia_2, and Microglia_3) with other cell types. Same cell-cell communication analysis procedures
255 were repeated for cone and rod sub-populations.
256

257 ## Results

258 **Construction and Analysis of Human Retinal scRNA-seq Library**

259 To investigate diabetic retinopathy progression, we performed scRNA-seq on thirteen human retina
260 samples encompassing three disease stages (nonDM, DM, DR). After stringent quality control and data
261 integration using scVI, we visualized retinal cell populations in UMAP visualization (Figure 2A),
262 identifying cone, rod, bipolar (BC), amacrine (AC), horizontal (HC), retinal ganglion (RGC), Müller glia
263 (MGC), astrocytes, microglia, and T cells (TC) by significant makers shown in Figure 2B. The
264 transcriptional profiles across nonDM, DM, and DR groups demonstrated consistent cell-type-specific
265 marker expression patterns, as visualized in Figure S1. This integration remained robust across both
266 living and post-mortem samples, enabling us to establish a reliable reference for cell-type composition
267 and disease-related changes. In total, rods represented the majority (>75% in most datasets), while other
268 cell types (e.g., microglia, MGC, BC) varied by disease stage (Figure S2). After the initial identification

269 of major retinal cell populations, we performed subtype annotation using known gene markers. The rod
270 population was further classified into Type1 Rod and Type2 Rod and mRod, an intermediate rod state
271 that shares characteristics of both Type1 and Type2 based on their differential gene expression profiles
272 (Figure 2C, D). For BCs, we identified multiple distinct subtypes (DB1-DB6, BB+GB, RB, FMB, IMB,
273 and OFFx) characterized by specific signatures as shown in the dot plot (Figure 2E, F).

274

275 **Identification of DR-Associated Retinal Cell Types Through Multi-Modal Computational**
276 **Analysis**

277 Although microglia have been centrally investigated in DR pathogenesis, we applied three independent
278 computational approaches (scDist, miloR, and Augur methods) to explore a wider array of cell types
279 significantly associated with DR progression. The distance-based scDist analysis revealed TC and
280 microglia as the most divergent populations (Figure 3A), while Augur analysis identified cone and TC
281 as the most discriminative cell types between conditions (Figure 3B). The neighborhood-enrichment
282 analysis using miloR highlighted significant alterations in rod populations between nonDM and DR
283 states, as evidenced by the differential abundance patterns in the UMAP visualization (Figure 3C, D).
284 Notably, BCs and MGCs emerged as potentially relevant populations by comprehensively considering
285 the results of the three methods.

286

287 **Microglial Heterogeneity and Gene Expression Patterns in Human Diabetic Retina**

288 To comprehensively characterize microglial heterogeneity, we performed analyses across two
289 dimensions: cell-type-specific transcriptional profiles and disease state-associated changes. This

290 approach uncovered three distinct yet coexisting microglial states (Microglia_1, Microglia_2,
291 Microglia_3) (Figure 4). Microglia_2 exhibits a homeostatic signature enriched for ribosomal and
292 cytoskeletal genes (e.g., *RPS, TMSB4X*), alongside complement components (*C1QA, C1QB, C1QC*) but
293 lacking strong inflammatory markers. In contrast, Microglia_1 shows a stress-response phenotype,
294 marked by elevated heat shock proteins (*HSPA1A/B*) and immediate early genes (*FOSB, EGR1*), while
295 retaining moderate inflammatory capabilities (*CCL3, CCL4*). Microglia_3 presents a fully inflammatory
296 profile with S100 proteins (*S100A8, S100A9*) and neutrophil-like mediators (*FCGR3B, PROK2*),
297 accompanied by downregulation of homeostatic and metabolic genes. Comparisons across disease stages
298 reveal that all three states persist throughout DR progression but shift in transcriptional intensity. NonDM
299 microglia maintain homeostatic phagocytic functions (*CD68, MARCO*), whereas DM microglia show
300 a transitional phenotype—undergoing partial metabolic reprogramming (e.g., upregulation
301 of *ACTB, TMSB4X*) and downregulation of immune modulators (*CD83, MS4A7*). By DR, a pronounced
302 inflammatory activation emerges, exemplified by chemokines (*CXCL8, CCL3/4*) and stress-response
303 genes (*HSPA1B*)—a shift from metabolic adaptation to robust immune engagement (Figure 5).

304 Microglial responses to diabetic stress involve complex interactions between different functional states
305 rather than simple phenotypic switches. To elucidate the functional modules driving these state
306 transitions, we employed three computational frameworks: Hotspot, hdWGCNA, and CoGAPS. Hotspot
307 identified a ribosomal/translation module (M1), an immune cell function module (M2+M4), and
308 an inflammatory/transcriptional regulation module (M3+M5+M6) (Figure 6A–C). Modules of similar
309 functions can be also detected and verified by hdWGCNA and CoGAPS. These computational patterns
310 showed remarkable alignment with our previously identified microglial states: Microglia_2 (homeostatic)
311 aligned with the ribosomal/translation module, Microglia_1 (stress-response) correlated with the

312 inflammatory/transcriptional modules (M3+M5+M6), and Microglia_3 (inflammatory/neutrophil-like)
313 mapped strongly to the immune function module (M2+M4).

314 Figure 6D demonstrates clear disease-specific patterns of module activation between nonDM and DM
315 group, illustrating the differences between DR-specific responses and general inflammatory patterns.
316 Core functional module M1 (ribosomal/translation) maintains stable expression between nonDM and DR
317 conditions, suggesting preserved protein synthesis machinery. M2, enriched in phagocytosis and
318 leukocyte migration, also shows no significant difference between nonDM and DR states, indicating that
319 basic immune surveillance functions remain constant. In contrast, Modules M3, M5, M6, and M7
320 demonstrate significant upregulation in DR compared to nonDM ($p < 0.0001$), while M4 shows moderate
321 but significant upregulation in DR ($p < 0.01$). The preservation of modules M1 and M2 alongside the
322 selective activation of M3, M4, M5, M6 and M7. This duality ensures that while essential cellular and
323 immune functions remain operational, the microglia engage in targeted inflammatory activities that likely
324 contribute to the pathogenesis and progression of diabetic retinopathy. Detailed analysis of Microglia
325 can be checked in supplementary file section A.

326

327 **Temporal Analysis Reveals Dynamic Differentiation Trajectories of Retinal Microglial Subtypes**

328 To investigate developmental relationships among microglial subtypes, we
329 performed CytoTRACE analysis across integrated (all samples), DR-specific, and nonDM-specific
330 datasets. In each scenario, Microglia_2 consistently emerged as the least differentiated state,
331 and Microglia_3 exhibited the highest differentiation status (Supplementary Figure S3). Independent
332 pseudotime analyses using Monocle2 and Monocle3 confirmed this hierarchy, revealing bifurcating

333 trajectories rooted in Microglia_2. Cells branch into two distinct lineages transitioning toward
334 either Microglia_1 or Microglia_3 (Figure 7A–D). To understand the molecular programs driving these
335 trajectories, we analyzed the temporal dynamics of previously identified Hotspot modules (Figure7 E,
336 F). The ribosomal/translation module (M1) exhibited a distinctive pattern in both conditions: an initial
337 high expression (>1.5) followed by sharp decline to around 0, after which DR condition showed a gradual
338 increase to approximately 1 and maintained this level. The immune surveillance module (M2) showed
339 remarkably stable low expression throughout pseudotime, with only a transient early activation spike at
340 the early time, indicating tight temporal control of baseline immune functions. The inflammatory
341 response modules (M3, M5, M6) demonstrated distinct temporal patterns between conditions. In nonDM,
342 M3 showed an initial increase and then maintained stable expression, while in DR it displayed a
343 consistent increasing trend throughout its extended trajectory reaching higher values. M5 and M6
344 exhibited stronger and more continuous increases in DR compared to nonDM, with DR keeping
345 progressive activation during the further time of the trajectory. M4, associated with immune receptor-
346 mediated signaling, showed a different pattern: while it displayed gradual increase in nonDM, in DR it
347 showed dynamic regulation with alternating increases and decreases beyond the nonDM endpoint,
348 suggesting ongoing immune receptor modulation rather than continuous activation. M7 showed distinct
349 activation patterns between nonDM and DR conditions. In nonDM, the module displayed a strong and
350 steady increase from negative values to reach higher positive values. In contrast, DR exhibited an overall
351 reduced activation magnitude throughout its extended trajectory. While both conditions showed initial
352 increases from negative values, DR maintained consistently lower levels compared to nonDM,
353 suggesting a dampened regulatory response in the disease state.

RNA velocity analysis supports these pseudotime findings. The vector field visualization in Figure 7G demonstrates clear directional flows originating from Microglia_2, with distinct streams leading to both Microglia_1 and Microglia_3. The speed plot shows the highest velocity magnitudes at the interfaces between states, particularly where Microglia_2 transitions toward Microglia_1 and Microglia_3. The acceleration map shows the peak acceleration at transition zones, while curvature shows the highest values specifically along the paths leading to Microglia_1, suggesting more complex transitional trajectories in this region. The curvature pattern indicates that cells undergo more dramatic directional changes during commitment to the stress-response state compared to other fate decisions (Figure 7H).

Transcriptional Networks Reveals Key Regulators in DR Pathogenesis

Through gene regulatory networks analysis, we identified critical TFs orchestrating microglial responses during DR progressions. Under DM conditions, the transcriptional regulatory landscape is dominated by top-ranked TFs (e.g., *ZNF585A, RFX2*, and *HDX*) that predominantly exert positive control over gene networks, while others (e.g., *GTF2IRD1, E2F3*) display negative associations, jointly shaping both activation and repression of regulatory circuits under diabetic stress (Supplementary Table S2, Figure 8B). Using RSS ranking and CSI module detection, we identified distinct transcriptional modules (Module 1–7, Supplementary Table S3), visualized in the correlation heatmap (Figure 8A). DM conditions exhibit a distinctive regulatory signature characterized by TFs predominantly from Module 4, while other Module 4 factors like *NFE2L1* and *RXRB* with lower rankings demonstrate that diabetic stress activates a specific subset of transcriptional regulators rather than uniformly engaging all Module 4 components.

375 In the nonDM setting, the TF landscape reflects a balanced homeostatic state, with *CEBPD* (-), *LMO2*
376 (+), and *NFE2L1*(+) as top regulators. This equilibrium of positive and negative regulators suggests
377 tightly controlled immune surveillance functions. NonDM-specific TFs predominantly cluster in Module
378 5, a module likely with the role of "non-diabetic injury response" featuring key regulators such as *E2F1*,
379 *RELA,* and *SPI1*. Rather than driving metabolic stress responses, these TFs appear to focus on cell cycle
380 regulation and baseline inflammatory mechanisms to handle general retinal challenges in the absence of
381 diabetic stress. The DR condition dramatically reconfigures the transcriptional landscape, with stress-
382 responsive factors *JUND*(+) and *FOS*(+) emerging as dominant regulators, alongside *ATF3*(+) and
383 *JUN*(+), forming a tightly coordinated immediate early response network. This stress-responsive
384 program is balanced by high-ranking negative regulators like *ETV6*(-) and *TCF4*(-), suggesting
385 sophisticated control of the inflammatory response. This coordinated system of activators and repressors,
386 operating at approximately twice the magnitude of nonDM regulators, demonstrates precise regulation
387 of the stress response in DR.

388

389 **Distinct Molecular Signatures and Disease-State Transitions in Retinal Photoreceptor Subtypes**

390 The integrated analysis of photoreceptor adaptations during DR reveals sophisticated cell type-specific
391 responses among two distinct rod subtypes and cones. For the rod, we identified two distinct rod subtypes
392 (Type1 Rod, Type2 Rod) and a transitional mRod population that shares features of both (Figure 8C, D).
393 The cell communication analysis of Type1 Rod and Type2 Rod is shown in supplementary Figure S4.
394 Type1 Rod exhibits a molecular program dedicated to maintaining retinal structural integrity and
395 synaptic function. This includes robust expression of adhesion molecules (e.g., *EXOC4, PCDH15*) and
396 cytoskeletal genes (*MYO9A, ANK3*), alongside visual function genes (*EYS, USH2A*) (Supplementary

Table S4). By contrast, Type2 Rod displays a metabolically specialized profile with high expression of mitochondrial electron transport chain components (*MT-ND1, MT-CO1*) and ATP synthesis genes (*MT-ATP6*), suggesting a role in modulating immune responses. Notably, this subtype engages in dual MIF-CD74-CD44/CXCR4 pathways while also receiving PTN-NCL signals from horizontal cells, indicating a balance between energy metabolism and immune modulation. Transition to the DM condition triggers a pronounced photoreceptor stress response in both rod subtypes (Supplementary Table S5, S6). Type1 Rod shows strong early-gene activation (*EGR1, JUNB, FOS*) and heat-shock protein expression (*HSPA1B*), while Type2 Rod simultaneously upregulates *RBM3* and *SAMD1*, retaining essential visual cycle genes (*NRL, SAG*). Cones demonstrate parallel, yet distinct, stress adaptations, featuring immediate early genes (*FOS/FOSB*), heat-shock proteins (*HSPH1*), and MAPK regulators (*DUSP1, DUSP6*). Progression to the DR state fosters further metabolic reprogramming across photoreceptors. Type1 Rod maintains structural integrity but elevates *RPS4Y1* and hypoxia-related pathways (*HIF1A-AS3*). Type2 Rod enhances mitochondrial gene expression (*MT-CO3, MT-ND3*) while activating immune-related features (*B2M, HLA-B*). Cones upregulate glycolytic enzymes (*PGK1, TPI1*) and stress mediators (*PRDX1*) through MIF signaling, echoing chronic inflammatory and oxidative-stress adaptation (Figure 8E). Notably, the nonDM state shows broader enrichment of photoreceptor structural genes, while the DR state features increased ribosomal and RNA-processing activity, reflecting an evolving balance between metabolic demands, inflammation, and retinal functional maintenance. Detailed analysis of photoreceptor can be checked in supplementary file section B.

Dynamic Remodeling of Neural-Immune Communication Networks in Diabetic Retinopathy

Through cell communication analysis, we uncovered complex intercellular signaling networks between

microglial subtypes and other retinal cells that undergo significant remodeling during DR progression. Our analysis identified four key signaling axes with distinct disease-state-specific activation patterns: the ANXA1-FPR1 pathway (regulated by *NR3C1, SP1*, and *STAT6*), the IL1B-IL1R2 pathway (controlled by *NFKB1, RELA*, and *STAT3*), the MIF-CD74-CXCR4 axis (modulated by *JUN, FOS*, and *HIF1A*), and the APP-CD74 pathway (regulated by *CEBPB, STAT1*, and *IRF1*). We first examined Microglia_1, Microglia_2, and Microglia_3, highlighting their roles as both sources and targets of intercellular signaling. Microglia_1 displayed condition-specific bidirectional signaling with Microglia_3, transitioning from ANXA1-FPR1 signaling in nonDM conditions to IL1B-IL1R2 signaling in DR, reflecting a shift from homeostasis to inflammation. Neuronal inputs to Microglia_1 also exhibited disease-state dependence: while MIF-CD74-CXCR4 signaling from RGCs and cones intensified in DR, MIF-CD74-CD44 signaling was more active in nonDM. Similarly, Microglia_2 emerged as an intermediary node, engaging in APP-CD74 signaling with RGCs and MGCs and participating in MIF-CD74-mediated communication with other microglial subtypes. This pathway demonstrated condition-specific patterns, with MIF-CD74-CD44 dominating in nonDM and MIF-CD74-CXCR4 becoming more active in DR. Figure 9A highlights these pathways, illustrating the progression from anti-inflammatory to pro-inflammatory signaling across the microglial network. This signaling plasticity enables microglia to adapt to pathological changes while maintaining essential functions.

Furthermore, we delineate the remodeling of photoreceptor communication networks during DR. In nonDM, cones engaged Microglia_1 via MIF-CD74-CD44. Rods demonstrated subtype-specific communication patterns: Type2 Rods received PTN-NCL signals from HCs and interacted with microglia via MIF-CD74-CD44, balancing energy metabolism and immune signaling. Type1 Rods maintained CADM1-CADM1 interactions with BCs to preserve synaptic architecture under stress. As DR progressed,

441 cones signal with BCs through NRG1-ERBB4 and NEGR1-NEGR1 pathways, transitioned to MIF-
442 CD74-CXCR4 signaling with microglia and established CNTN1-NRCAM connections with RGCs,
443 underscoring their role in adapting to retinal dysfunction. Building on these findings, Figure 9B integrates
444 data from Supplementary Figures S4–S6, presenting a comprehensive neural-immune network in the
445 human retina under DR conditions.
446

447 **Discussion**

448 The advent of single-cell omics has significantly advanced our understanding of the pathological
449 mechanisms underlying DR [8]. However, significant gaps persist, particularly the lack of a
450 comprehensive analysis of human DR retina samples. While animal models, including diabetic mice and
451 non-human primates, have provided valuable insights [32-34], they fail to replicate the complexity of
452 human DR pathogenesis due to species-specific differences. Recent efforts have partially addressed these
453 gaps through single-cell analyses of human-derived tissues, such as PDR-fibrovascular membranes or
454 blood mononuclear cells [35, 36]. However, the lack of studies encompassing the retina limits our ability
455 to fully unravel the intricate cellular interactions and molecular mechanisms of DR in human.

456 Our study addresses these limitations by analyzing thirteen fresh human retinal samples categorized into
457 three groups: DR, DM, and nonDM. Microglia, as the key mediator of retinal inflammation [37, 38],
458 present a unique challenge in distinguishing DR-specific responses from general inflammatory patterns,
459 given their activation in various retinal pathologies. To resolve this, we designed an innovative approach
460 using fresh retinal samples from living donors, leveraging those with general inflammatory profiles as
461 controls. This approach enabled us to capture DR-specific molecular signatures while accounting for
462 background inflammation, clarifying microglial dynamics in DR progression.

463 The molecular heterogeneity and functional dynamics of retinal microglia in DR are not fully understood
464 due to insufficient comprehensive human retinal studies [37]. Traditionally described using the M1/M2
465 dichotomy, recent findings suggest that microglial activation spans a continuous spectrum rather than
466 being defined by discrete phenotypes [37, 39]. Through integrated transcriptional profiling of fresh
467 human retinal samples across DR progression, our analysis identifies three distinct microglial states:
468 Microglia_2, a homeostatic state essential for retinal integrity; Microglia_1, a hybrid stress-response
469 phenotype; and Microglia_3, a fully activated inflammatory state. These states persist throughout DR
470 progression, exhibiting dynamic functional adaptation mainly through transcriptional reprogramming in
471 early disease stages, with molecular changes surpassing relative changes in subtype populations. This
472 study provides the first comprehensive characterization of microglial state transitions along a continuous
473 spectrum in human DR progression at single-cell resolution, revealing three distinct functional states that
474 coexist across disease conditions.

475 In nonDM conditions, microglia predominantly maintain a homeostatic phenotype, as evidenced by
476 upregulation of phagocytic (*CD68, MARCO*) and tissue maintenance (*PLTP, STAB1*) genes. This aligns
477 with the Microglia_2 signature, marked by the expression of ribosomal proteins and cytoskeletal genes
478 that support active tissue surveillance and minimize retinal damage. Upon transitioning to DM, microglia
479 exhibit a partial stress-response program—downregulating certain immune modulators (*CD83, MS4A7*)
480 while upregulating cytoskeletal components (*ACTB, TMSB4X*)—suggesting a metabolic reprogramming
481 phase that balances tissue integrity with incipient inflammatory readiness. By the DR stage, a strongly
482 inflammatory phenotype emerges, culminating in the pronounced activation of chemokines and
483 immediate early genes. This is consistent with Microglia_3's robust inflammatory profile. Importantly,
484 this shift does not require a complete population turnover: all three microglial states—homeostatic,

transitional/stress-response, and inflammatory—remain detectable, highlighting microglial plasticity in adapting to progressive diabetic stress.

Using CSI module detection, we identified TF modules that related to the dynamic reconfiguration of microglial transcriptional networks, enabling microglia to balance homeostatic maintenance with robust stress and inflammatory responses during DR progression. Trajectory analysis further reveals that Microglia_2 represents a progenitor-like state that can differentiate into either stress-response (Microglia_1) or inflammatory (Microglia_3) phenotypes, with key transcription factors showing distinct expression gradients along developmental paths. The integrated analysis of velocity vectors and TF expression reveals Microglia_2 as a critical decision point in microglial state transitions. Dynamics of microglia states during DR progression are governed by sophisticated transcriptional programs organized into distinct functional modules. Core homeostatic functions, such as ribosomal/translation (M1) and immune surveillance (M2) modules, remain stable across disease states, while inflammatory and stress-response modules (M3, M5, M6) exhibit significant activation in DR. This modular organization enables microglia to balance tissue maintenance with adaptive immune responses under pathological conditions. Temporal dynamics further reveal DR-specific recovery of protein synthesis machinery (M1) and sustained activation of inflammatory pathways (M3), highlighting an evolving immune response rather than simple sustained activation. These findings underscore the remarkable plasticity of microglia in adapting to diabetic stress while maintaining essential functions.

Moreover, we identified distinct cellular populations undergoing substantial reprogramming during DR progression. Photoreceptors demonstrated high discriminative power between disease states, with two distinct rod subtypes emerging: Type2 Rods showing metabolic specialization and immune modulation, and Type1 Rods maintaining structural integrity through adhesion molecules and ion channels. Using

507 cell communication analysis, we reveal the sophisticated coordination between neural and immune cells
508 in the retina during DR progression. Dynamic remodeling of microglial communication networks during
509 DR progression highlights shifts from homeostatic to inflammatory signaling (e.g., ANXA1-FPR1 to
510 IL1B-IL1R2). Notably, the MIF-CD74-CXCR4 axis facilitated the integration of neural-derived signals
511 and immune responses, enabling microglia to balance baseline functions with emerging inflammatory
512 pathways.

513 While our study provides insights into DR progression, we acknowledge several limitations. The
514 relatively small sample size may limit statistical power for certain comparisons. However, this limitation
515 reflects the challenges in acquiring human retina samples, especially from DR patients. The human retina
516 is exceptionally rare and difficult to obtain due to several factors: (1) the limited availability of donor
517 tissue meeting specific disease criteria, (2) the critical requirement for minimal post-mortem intervals to
518 maintain RNA quality, and (3) the ethical and logistical complexities of collecting samples from living
519 donors during surgery. Despite these constraints, our study represents one of the largest single-cell
520 analyses of human retina in DR research to date. The inclusion of both living donor and post-mortem
521 specimens with careful processing time control helps mitigate some limitations while maintaining data
522 quality. Future studies with larger sample sizes would be valuable to validate our findings, though the
523 inherent challenges of human retinal tissue collection will likely continue to pose significant barriers to
524 large-scale analyses.

525 Our findings provide critical insights into DR pathogenesis, highlighting three distinct microglial states
526 and their roles in disease progression. We demonstrate that DR involves complex coordination between
527 immune responses and neuronal changes, which precede visible vascular alterations. The identification
528 of microglial states and their developmental trajectories, along with photoreceptor-specific adaptations,

reveals key mechanisms driving DR. These insights suggest that therapeutic strategies should focus on modulating microglial functional states, rather than targeting specific populations. Understanding these transcriptional programs may facilitate early intervention to prevent irreversible inflammatory damage and provide new treatment options for DR and other neurodegenerative diseases.

Statements and Declarations

Data availability

The single-cell RNA sequencing data generated in this study have been deposited in Figshare with the DOI: 10.6084/m9.figshare.28228949 and will be publicly available upon publication.

Author information

Authors and Affiliations

Nottingham Ningbo China Beacons of Excellence Research and Innovation Institute, University of Nottingham Ningbo China, Ningbo, China, 315100

Luning Yang, Sen Lin, Yiwen Tao, Qi Pan, Tengda Cai, Weihua Meng

Department of Ophthalmology, Lihuili Hospital affiliated with Ningbo University, Ningbo, China, 315040

Yunyan Ye

Department of Cardiology, Lihuili Hospital affiliated with Ningbo University, Ningbo, China, 315040

Jianhui Liu

Ningbo Institute of Innovation for Combined Medicine and Engineering, The Affiliated Li Huili Hospital, Ningbo University, Ningbo, China, 315201

Yang Zhou

Department of Ophthalmology, The Affiliated Ningbo Eye Hospital of Wenzhou Medical University, Ningbo, China, 315040

Quanyong Yi, Yongqing Shao

PAPRSB Institute of Health Sciences, Universiti Brunei Darussalam, Bandar Seri, Begawan, BE1410, Brunei Darussalam

Zen Haut Lu, Lie Chen

Centre for Public Health, Institute of Clinical Science, Queen's University Belfast, Block B, Royal Hospital, Grosvenor Road, Belfast, Northern Ireland, BT12 6BA

Gareth McKay

School of Mathematical Sciences, University of Nottingham Ningbo China, Ningbo, China, 315100

Richard Rankin

Authors' Contributions

LY drafted the paper and performed the analysis. SL, YT, QP, TC contributed to data formatting and correction. YY, JL, YZ, QY, ZL, LC, GM, and RR provided comments on the paper. YS, and WM organized the project and provided comments.

Acknowledgment

This study was mainly funded by the Pioneer and Leading Goose R&D Program of Zhejiang Province 2023 with reference number 2023C04049 and Ningbo International Collaboration Program 2023 with reference number 2023H025.

Corresponding authors

Correspondence to Dr. Weihua Meng and Dr. Yongqing Shao.

Consent to Publish

All authors have consent for publication.

Conflict of Interest

The authors have no conflicts of interest to disclose.

Ethics approval

This study was approved by the Ethics Committee of the University of Nottingham Ningbo China; The Lihuili Hospital affiliated with Ningbo University; The Affiliated Ningbo Eye Hospital of Wenzhou Medical University.

References

1. Ji L, Tian H, Webster KA, Li W: **Neurovascular regulation in diabetic retinopathy and emerging therapies**. *Cellular and Molecular Life Sciences* 2021, **78**:5977-5985.
2. Zhou B, Rayner AW, Gregg EW, Sheffer KE, Carrillo-Larco RM, Bennett JE, Shaw JE, Paciorek CJ, Singleton RK, Pires AB: **Worldwide trends in diabetes prevalence and treatment from 1990 to 2022: a pooled analysis of 1108 population-representative studies with 141 million participants**. *The Lancet* 2024, **404**(10467):2077-2093.
3. Teo ZL, Tham Y-C, Yu M, Chee ML, Rim TH, Cheung N, Bikbov MM, Wang YX, Tang Y, Lu Y: **Global prevalence of diabetic retinopathy and projection of burden through 2045: systematic review and meta-analysis**. *Ophthalmology* 2021, **128**(11):1580-1591.
4. Tomita Y, Lee D, Tsubota K, Negishi K, Kurihara T: **Updates on the current treatments for diabetic retinopathy and possibility of future oral therapy**. *Journal of clinical medicine* 2021, **10**(20):4666.
5. Cheung N, Wong IY, Wong TY: **Ocular anti-VEGF therapy for diabetic retinopathy: overview of clinical efficacy and evolving applications**. *Diabetes care* 2014, **37**(4):900-905.
6. Tang Q, Buonfiglio F, Böhm EW, Zhang L, Pfeiffer N, Korb CA, Gericke A: **Diabetic Retinopathy: New Treatment Approaches Targeting Redox and Immune Mechanisms**. *Antioxidants* 2024, **13**(5):594.
7. Duh EJ, Sun JK, Stitt AW: **Diabetic retinopathy: current understanding, mechanisms, and treatment strategies**. *JCI insight* 2017, **2**(14).
8. Zhang X, Zhang F, Xu X: **Single-cell RNA sequencing in exploring the pathogenesis of diabetic retinopathy**. *Clinical and Translational Medicine* 2024, **14**(7):e1751.
9. Wang J, Sun H, Mou L, Lu Y, Wu Z, Pu Z, Yang M-m: **Unveiling the molecular complexity of proliferative diabetic retinopathy through scRNA-seq, AlphaFold 2, and machine learning**. *Frontiers in Endocrinology* 2024, **15**:1382896.
10. Haliyur R, Parkinson D, Xu J, Li Q, Huang Y, Liu J, Ma F, Gudjonsson J, Rao R: **Liquid biopsy for proliferative diabetic retinopathy: single-cell transcriptomics (scRNA-seq) of human vitreous reveals inflammatory T cell signature**. *Investigative Ophthalmology & Visual Science* 2024, **65**(7):935-935.
11. Hu Q, Zhang X, Peng H, Guan J, Huang Z, Jiang B, Sun D: **A New Modulator of Neuroinflammation in Diabetic Retinopathy: USP25**. *Inflammation* 2024:1-16.
12. Mizee MR, Miedema SS, van der Poel M, Adelia, Schuurman KG, van Strien ME, Melief J, Smolders J, Hendrickx DA, Heutinck KM: **Isolation of primary microglia from the human post-mortem brain: effects of ante-and post-mortem variables**. *Acta neuropathologica communications* 2017, **5**:1-14.
13. Guo L, Choi S, Bikkannavar P, Cordeiro MF: **Microglia: key players in retinal ageing and neurodegeneration**. *Frontiers in Cellular Neuroscience* 2022, **16**:804782.
14. Ramirez AI, de Hoz R, Salobrar-Garcia E, Salazar JJ, Rojas B, Ajoy D, López-Cuenca I, Rojas P, Triviño A, Ramírez JM: **The role of microglia in retinal neurodegeneration: Alzheimer's disease, Parkinson, and glaucoma**. *Frontiers in aging neuroscience* 2017, **9**:214.
15. Wang SK, Cepko CL: **Targeting microglia to treat degenerative eye diseases**. *Frontiers in immunology* 2022, **13**:843558.

16. Hao Y, Stuart T, Kowalski MH, Choudhary S, Hoffman P, Hartman A, Srivastava A, Molla G, Madad S, Fernandez-Granda C: **Dictionary learning for integrative, multimodal and scalable single-cell analysis**. *Nature biotechnology* 2024, **42**(2):293-304.
17. Wolf FA, Angerer P, Theis FJ: **SCANPY: large-scale single-cell gene expression data analysis**. *Genome biology* 2018, **19**:1-5.
18. Gayoso A, Lopez R, Xing G, Boyeau P, Valiollah Pour Amiri V, Hong J, Wu K, Jayasuriya M, Mehlman E, Langevin M: **A Python library for probabilistic analysis of single-cell omics data**. *Nature biotechnology* 2022, **40**(2):163-166.
19. Nicol PB, Paulson D, Qian G, Liu XS, Irizarry R, Sahu AD: **Robust identification of perturbed cell types in single-cell RNA-seq data**. *Nature Communications* 2024, **15**(1):7610.
20. Skinnider MA, Squair JW, Kathe C, Anderson MA, Gautier M, Matson KJ, Milano M, Hutson TH, Barraud Q, Phillips AA: **Cell type prioritization in single-cell data**. *Nature biotechnology* 2021, **39**(1):30-34.
21. Dann E, Henderson NC, Teichmann SA, Morgan MD, Marioni JC: **Differential abundance testing on single-cell data using k-nearest neighbor graphs**. *Nature biotechnology* 2022, **40**(2):245-253.
22. Yu G, Wang L-G, Han Y, He Q-Y: **clusterProfiler: an R package for comparing biological themes among gene clusters**. *Omics: a journal of integrative biology* 2012, **16**(5):284-287.
23. Fan C, Chen F, Chen Y, Huang L, Wang M, Liu Y, Wang Y, Guo H, Zheng N, Liu Y: **irGSEA: the integration of single-cell rank-based gene set enrichment analysis**. *Briefings in Bioinformatics* 2024, **25**(4):bbae243.
24. Morabito S, Reese F, Rahimzadeh N, Miyoshi E, Swarup V: **hdWGCNA identifies co-expression networks in high-dimensional transcriptomics data**. *Cell reports methods* 2023, **3**(6).
25. Andreatta M, Carmona SJ: **UCell: Robust and scalable single-cell gene signature scoring**. *Computational and structural biotechnology journal* 2021, **19**:3796-3798.
26. Kang M, Armenteros JJA, Gulati GS, Gleyzer R, Avagyan S, Brown EL, Zhang W, Usmani A, Earland N, Wu Z: **Mapping single-cell developmental potential in health and disease with interpretable deep learning**. *bioRxiv* 2024:2024.2003. 2019.585637.
27. Trapnell C, Cacchiarelli D, Grimsby J, Pokharel P, Li S, Morse M, Lennon NJ, Livak KJ, Mikkelsen TS, Rinn JL: **The dynamics and regulators of cell fate decisions are revealed by pseudotemporal ordering of single cells**. *Nature biotechnology* 2014, **32**(4):381-386.
28. Qiu X, Zhang Y, Martin-Rufino JD, Weng C, Hosseinzadeh S, Yang D, Pogson AN, Hein MY, Min KHJ, Wang L: **Mapping transcriptomic vector fields of single cells**. *Cell* 2022, **185**(4):690-711. e645.
29. La Manno G, Soldatov R, Zeisel A, Braun E, Hochgerner H, Petukhov V, Lidschreiber K, Kastriti ME, Lönnerberg P, Furlan A: **RNA velocity of single cells**. *Nature* 2018, **560**(7719):494-498.
30. Aibar S, González-Blas CB, Moerman T, Huynh-Thu VA, Imrichova H, Hulselmans G, Rambow F, Marine J-C, Geurts P, Aerts J: **SCENIC: single-cell regulatory network inference and clustering**. *Nature methods* 2017, **14**(11):1083-1086.
31. Jin S, Plikus MV, Nie Q: **CellChat for systematic analysis of cell–cell communication**

673 **from single-cell transcriptomics**. *Nature Protocols* 2024:1-40.
674 32. Xiao Y, Hu X, Fan S, Zhong J, Mo X, Liu X, Hu Y: **Single-cell transcriptome profiling**
675 **reveals the suppressive role of retinal neurons in microglia activation under diabetes**
676 **mellitus**. *Frontiers in Cell and Developmental Biology* 2021, **9**:680947.
677 33. Niu T, Fang J, Shi X, Zhao M, Xing X, Wang Y, Zhu S, Liu K: **Pathogenesis study based on**
678 **high-throughput single-cell sequencing analysis reveals novel transcriptional**
679 **landscape and heterogeneity of retinal cells in type 2 diabetic mice**. *Diabetes* 2021,
680 **70**(5):1185-1197.
681 34. Van Hove I, De Groef L, Boeckx B, Modave E, Hu T-T, Beets K, Etienne I, Van Bergen T,
682 Lambrechts D, Moons L: **Single-cell transcriptome analysis of the Akimba mouse**
683 **retina reveals cell-type-specific insights into the pathobiology of diabetic**
684 **retinopathy**. *Diabetologia* 2020, **63**:2235-2248.
685 35. Hu Z, Mao X, Chen M, Wu X, Zhu T, Liu Y, Zhang Z, Fan W, Xie P, Yuan S: **Single-cell**
686 **transcriptomics reveals novel role of microglia in fibrovascular membrane of**
687 **proliferative diabetic retinopathy**. *Diabetes* 2022, **71**(4):762-773.
688 36. Liao D, Fan W, Li N, Li R, Wang X, Liu J, Wang H, Hou S: **A single cell atlas of circulating**
689 **immune cells involved in diabetic retinopathy**. *Iscience* 2024, **27**(2).
690 37. Wang Y, Yang X, Zhang Y, Hong L, Xie Z, Jiang W, Chen L, Xiong K, Yang S, Lin M: **Single-**
691 **cell RNA sequencing reveals roles of unique retinal microglia types in early diabetic**
692 **retinopathy**. *Diabetology & Metabolic Syndrome* 2024, **16**(1):49.
693 38. Yuan T, Dong L, Pearsall EA, Zhou K, Cheng R, Ma J-X: **The protective role of microglial**
694 **pparα in diabetic retinal neurodegeneration and neurovascular dysfunction**. *Cells*
695 2022, **11**(23):3869.
696 39. Hu A, Schmidt MH, Heinig N: **Microglia in retinal angiogenesis and diabetic**
697 **retinopathy**. *Angiogenesis* 2024:1-21.
698
699

Figures

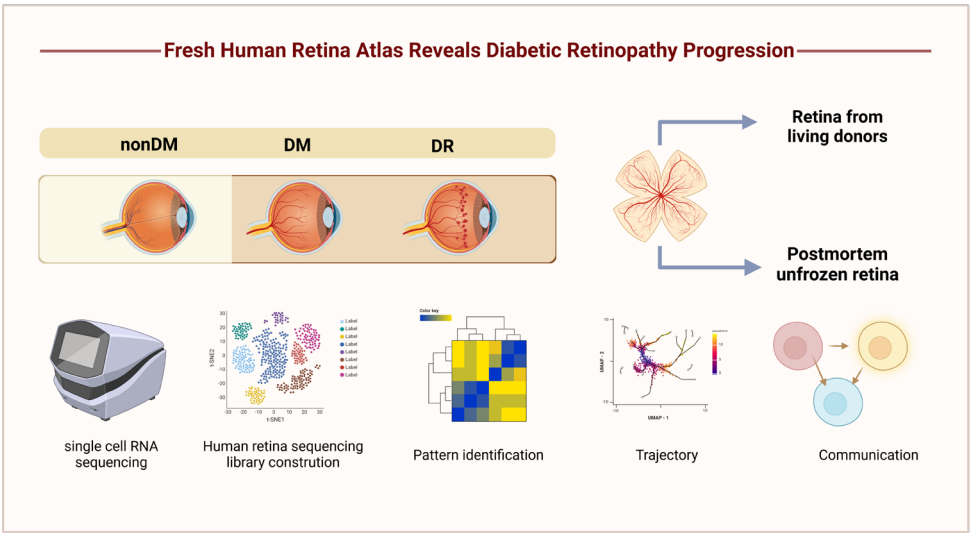

Fig1 Single-cell transcriptomic profiling of fresh human retina reveals molecular signatures of diabetic retinopathy progression.

Schematic overview of the experimental and analytical workflow. Human retinal samples were collected from nonDM, DM, and DR conditions, comprising both living donor tissue (processed within 10 minutes of surgical enucleation) and temperature-controlled post-mortem specimens (processed within 12 hours). Single-cell RNA sequencing was performed followed by comprehensive computational analyses including library construction, pattern identification, trajectory inference, and cell-cell communication analysis. This integrated approach enables detailed characterization of transcriptional changes and cellular interactions during DR progression. This figure was created using BioRender.

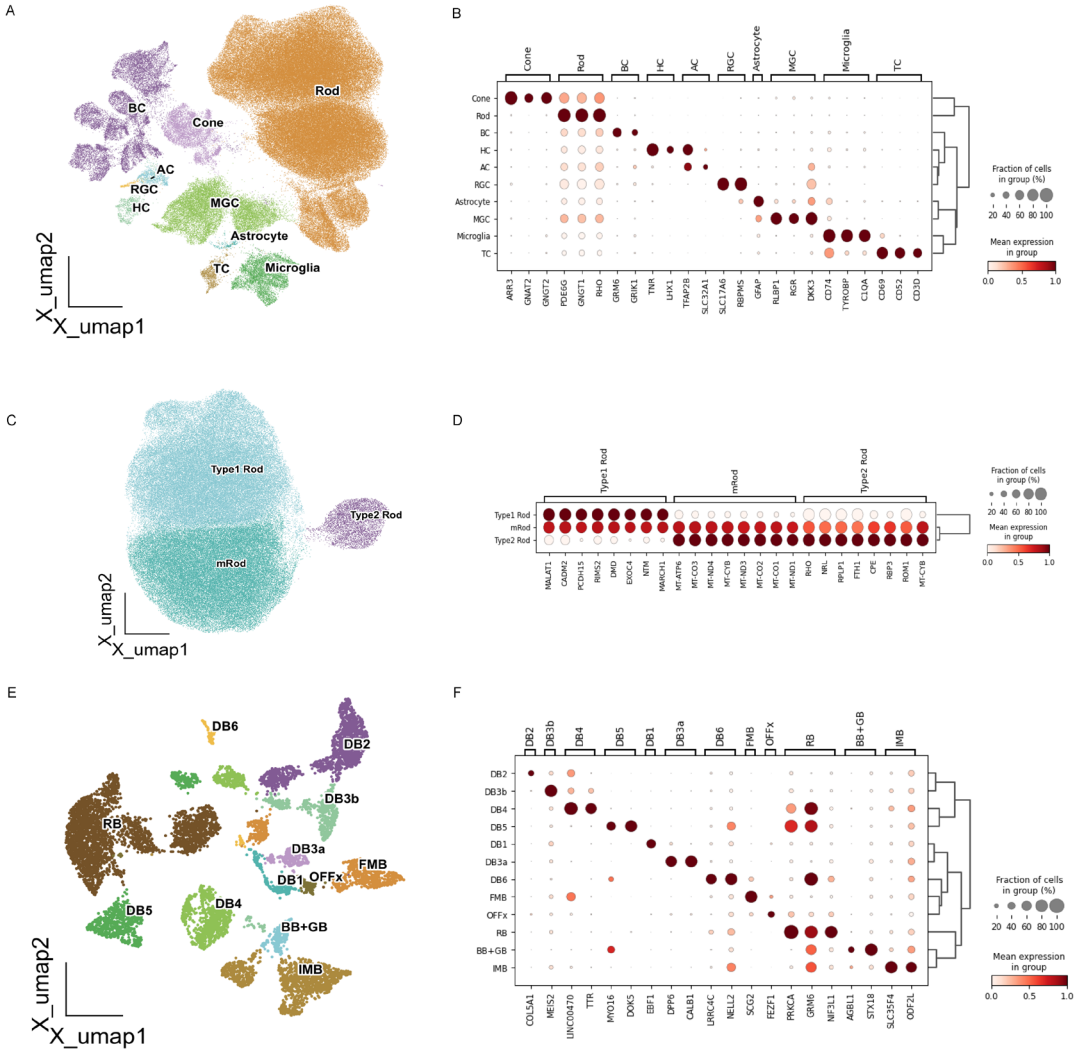

712

713 **Fig2** Single-cell RNA sequencing reveals cellular heterogeneity in the human retina.

714 (A) UMAP visualization of major retinal cell types identified from scRNA-seq data. Cell types are

715 color-coded and labeled. BC: Bipolar cell, MGC: Müller glia cell, TC: T cell, AC: Amacrine cell, RGC:

716 Retinal ganglion cell, HC: Horizontal cell.

717 (B) Dot plot of selected marker genes for major retinal cell types and T cells. Dot size represents the

718 percentage of cells in each population expressing the gene, while color intensity indicates the normalized

719 average expression level.

720 (C) UMAP plots highlighting rod photoreceptor subtypes.

721 (D) Dot plot of selected marker genes for rod subtypes. Dot size represents the percentage of cells in

722 each population expressing the gene, while color intensity indicates the normalized average expression

723 level.

724 (E) UMAP visualization of bipolar cell subtypes.

725 (F) Dot plot of selected marker genes for bipolar subtypes. Dot size represents the percentage of cells in

726 each population expressing the gene, while color intensity indicates the normalized average expression

727 level.

728

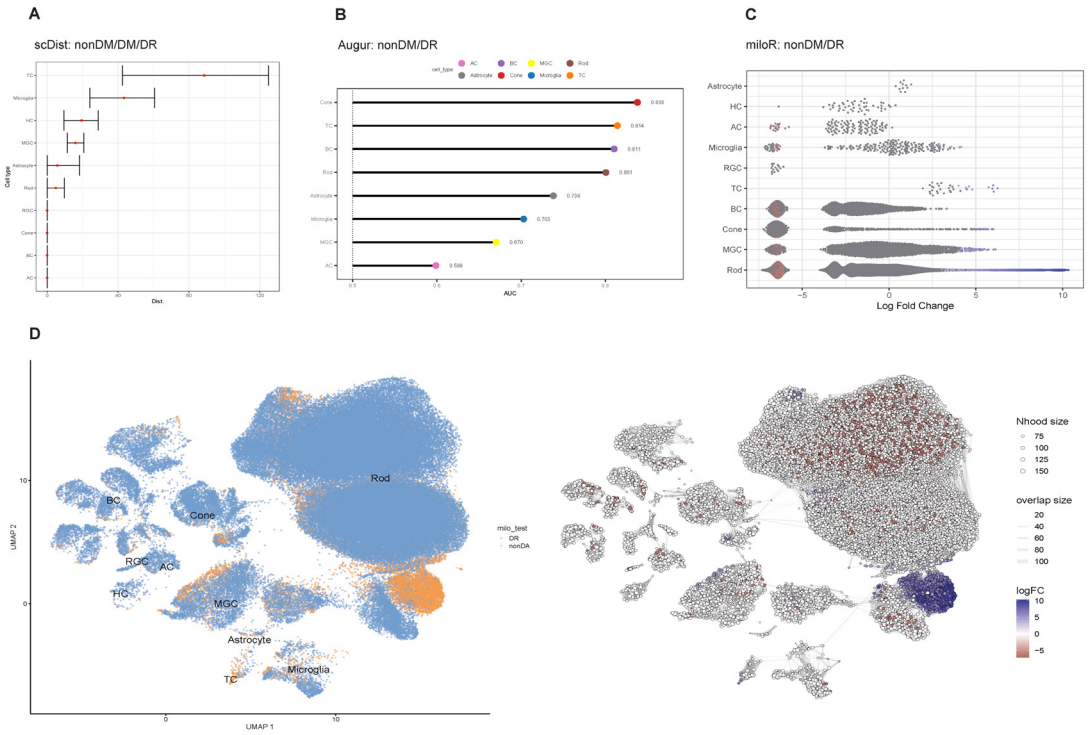

Fig3 Differential abundance analysis reveals cell type-specific changes across diabetic retinopathy progression.

(A) scDist analysis quantifies the differential abundance of retinal cell populations across non-diabetic (nonDM), diabetic (DM), and diabetic retinopathy (DR) conditions. The x-axis shows the distance metric representing cell type-specific abundance shifts, and error bars indicate variability across replicates.

(B) Augur analysis ranks retinal cell populations by their predictive accuracy (AUC) in distinguishing nonDM and DR samples. Higher AUC scores correspond to greater changes in population frequency during disease progression. Each dot represents a specific cell type, color-coded by identity.

(C) MiloR differential abundance testing compares cell population frequencies between nonDM and DR conditions. The x-axis displays log fold changes for each major cell type, with positive values indicating enrichment in nonDM and negative values indicating depletion in nonDM (enrichment in DR)

(D) UMAP visualization of MiloR results maps the spatial distribution of differentially abundant retinal

742 cell populations. The left panel shows the overall clustering of retinal cell types, with cells colored by
743 condition (blue: DR; orange: nonDM). The right panel highlights significant regions of differential
744 abundance, where log fold changes are represented by a gradient (blue: increased abundance in nonDM;
745 red: decreased abundance in nonDM, corresponding to enrichment in DR). Node sizes reflect
746 neighborhood size, and edge overlap magnitudes indicate spatial proximity between clusters.
747

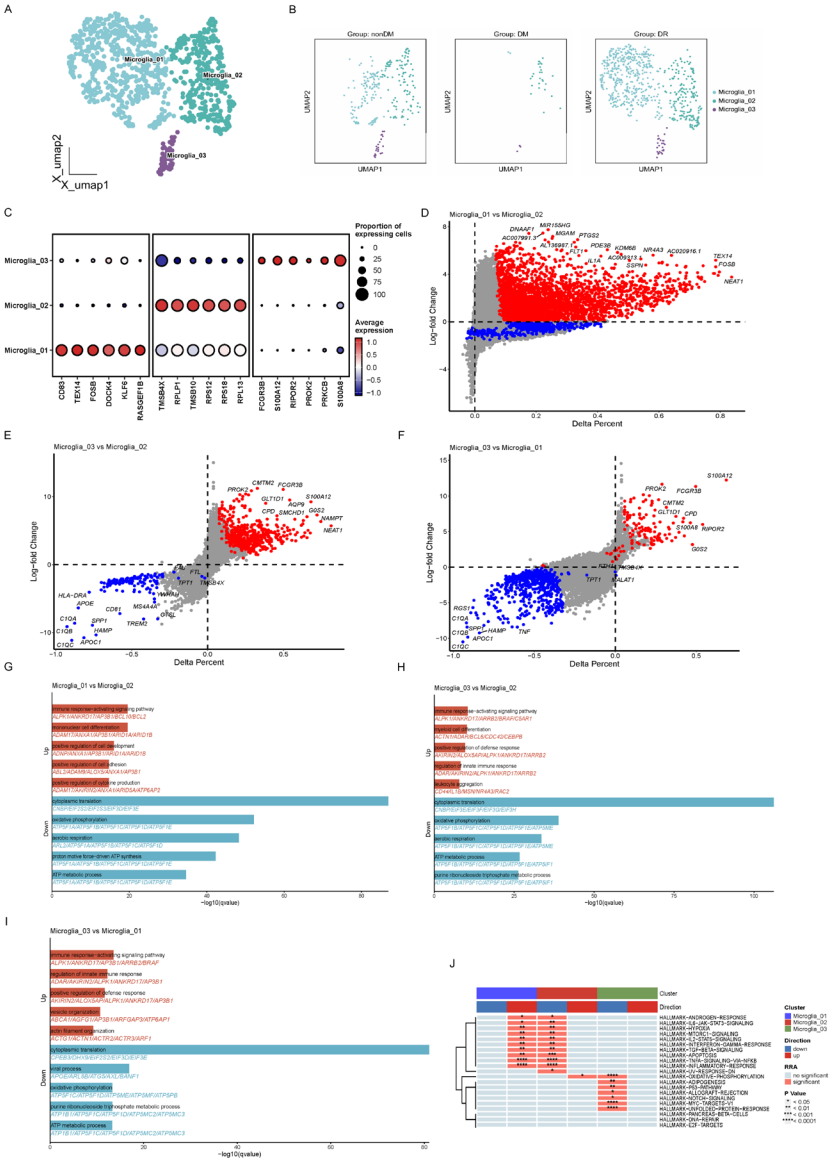

Fig4 Characterization and comparative analysis of microglial subtypes.

(A) UMAP visualization of microglial subtypes, showing three distinct clusters: Microglia_1, Microglia_2, and Microglia_3.

(B) UMAP projections comparing the distribution of microglial subtypes across nonDM (non-diabetic), DM (diabetic), and DR (diabetic retinopathy) conditions.

(C) Dot plot showing the expression of differential expressed genes across the three microglial subtypes. The size of the dots represents the proportion of expressing cells, and the color indicates average expression levels.

(D-F) Differential gene expression analysis between microglial subtypes using diagonal scatter plots. (D) Gene expression comparison between Microglia_1 and Microglia_2, (E) Microglia_3 and Microglia_2, and (F) Microglia_3 and Microglia_1. For all plots, x-axis represents delta percentage of gene expression (difference in the proportion of cells expressing a gene between the two subtypes), y-axis shows the log2 fold change (LogFC) in expression levels. Red points indicate significantly upregulated genes (LogFC > 0.1, adjusted p-value < 0.05) in the first mentioned subtype, blue points indicate significantly downregulated genes (LogFC < -0.1, adjusted p-value < 0.05) in the first mentioned subtype. Key marker genes are labeled.

(G-I) GOenrichment analysis showing significantly enriched biological processes between (G) Microglia_1 vs Microglia_2, (H) Microglia_3 vs Microglia_2, and (I) Microglia_3 vs Microglia_1. Bar length represents -log10(qvalue), with red bars indicating upregulated pathways and blue bars showing downregulated pathways in each comparison.

(J) Heatmap of integrated gene set enrichment analysis (irGSEA) results showing pathway activities across the three microglial subtypes. The top bar indicates cluster identity, and the second bar shows direction of regulation (blue: down, red: up). Significance levels are indicated by asterisks (* $p < 0.05$, ** $p < 0.01$, *** $p < 0.001$, **** $p < 0.0001$).

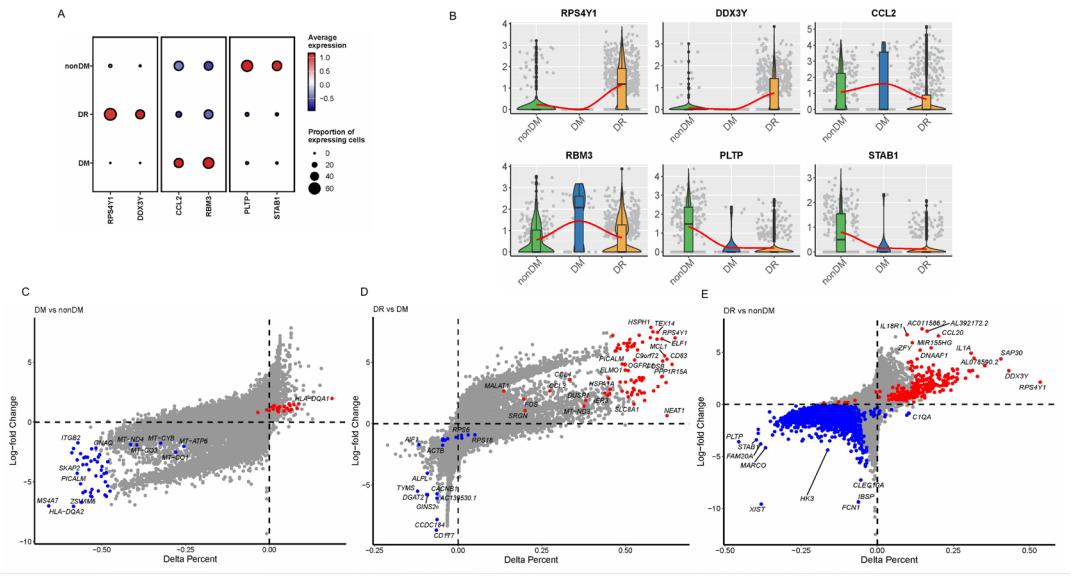

Fig5 Transcriptional and functional changes in microglia during diabetic retinopathy progression

(A) Dot plot showing expression of differential expressed genes across nonDM, DM, and DR conditions. Dot size represents the proportion of expressing cells, and color intensity indicates average expression level.

(B) Violin plots showing expression dynamics of six representative genes (RPS4Y1, DDX3Y, CCL2, RBM3, PLTP, STAB1) across disease progression (nonDM, DM, DR). Red lines indicate expression trends, and individual dots represent each individual cell.

(C-E) Differential gene expression analysis between disease progression (nonDM, DM, DR) using diagonal scatter plots. (C) Gene expression comparison between DM and nonDM, (D) DR and DM, and (E) DR and nonDM. For all plots, x-axis represents delta percentage of gene expression (difference in the proportion of cells expressing a gene between the two conditions), y-axis shows the log2 fold change (LogFC) in expression levels. Red points indicate significantly upregulated genes (LogFC > 0.1, adjusted p-value < 0.05) in the first mentioned condition group, blue points indicate significantly downregulated genes (LogFC < -0.1, adjusted p-value < 0.05) in the first mentioned condition group. Key marker genes are labeled.

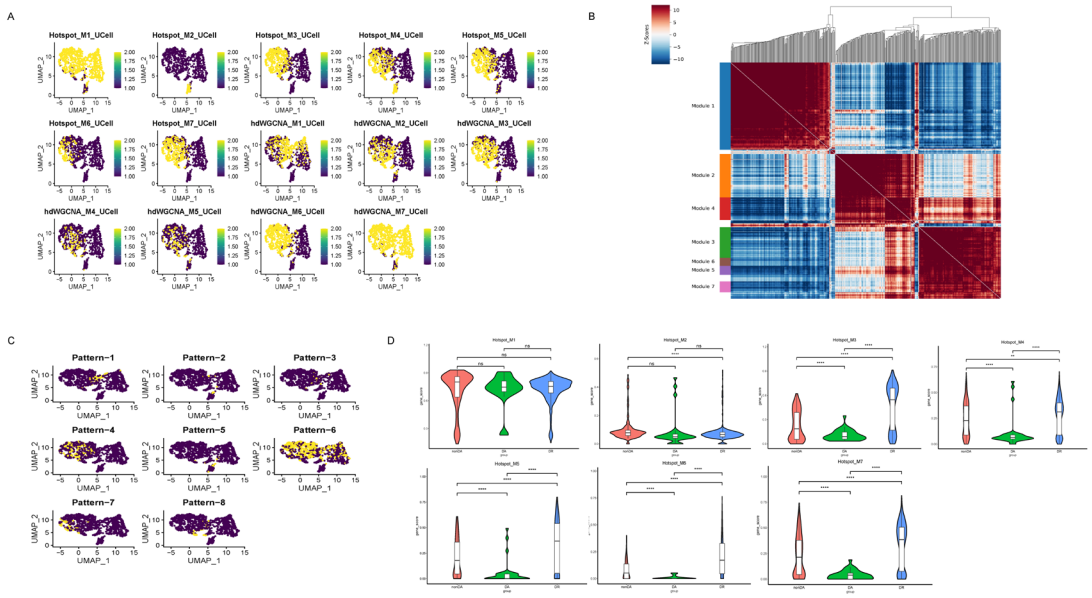

Fig6 Transcriptional modules identified through integrated computational approaches in retinal microglia.

(A) UMAP visualization of Hotspot modules (Hotspot_M1-M7) and hdWGCNA modules (hdWGCNA_M1-M7) identified in microglia populations. Color intensity indicates module activity scores.

(B) Correlation heatmap showing relationships between identified Hotspot modules. Sidebar colors represent different module classifications. Color scale indicates correlation strength (red: positive correlation, blue: negative correlation)

(C) UMAP visualization of eight distinct CoGAPS patterns (Pattern-1 to Pattern-8) identified in microglia

(D) Violin plots showing the distribution of Hotspot module scores across microglial populations in different conditions. Each panel represents a distinct module, with colors indicating different DR conditions (red, green, and blue). Statistical significance is indicated by asterisks (ns $p>0.05$, ** $p < 0.01$, **** $p < 0.0001$).

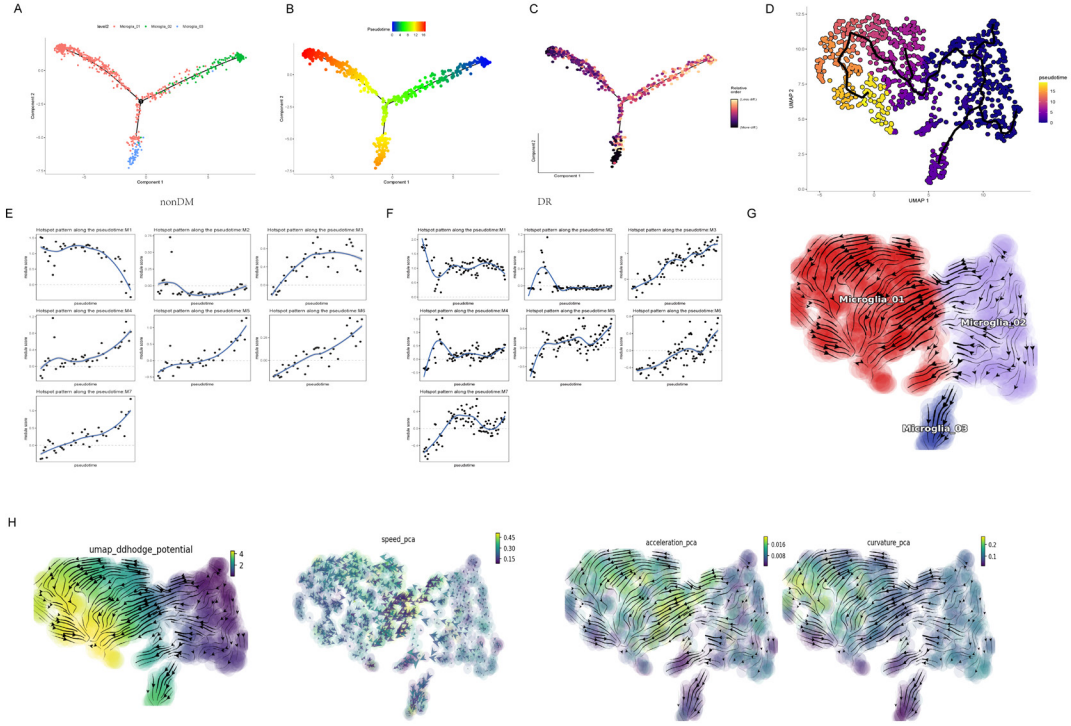

Fig7 Developmental trajectory dynamics of microglial subtypes during DR progression.

(A-C) Monocle2 trajectory analysis showing bifurcating developmental paths originating from Microglia_2. (A) Cells colored by microglial subtypes (Microglia_1, Microglia_2, Microglia_3), (B) by pseudotime progression, and (C) by CytoTRACE2 differentiation potential analysis, identifying Microglia_2 as the least differentiated state.

(D) Monocle3 UMAP visualization of microglial populations colored by pseudotime values, indicating developmental progression.

(E-F) Temporal dynamics of Hotspot module scores along Monocle3 pseudotime trajectories in (E) nonDM and (F) DR conditions. Each plot shows module activity patterns (M1-M7) with dots representing individual cells and smoothed lines indicating temporal trends.

(G) Dynamo RNA velocity analysis showing directional flows between microglial states. Arrows indicate predicted cell state transitions based on splicing dynamics.

(H) Dynamo-derived velocity metrics (ddhodge potential, speed, acceleration, curvature) visualized on UMAP, revealing regulatory dynamics during state transitions.

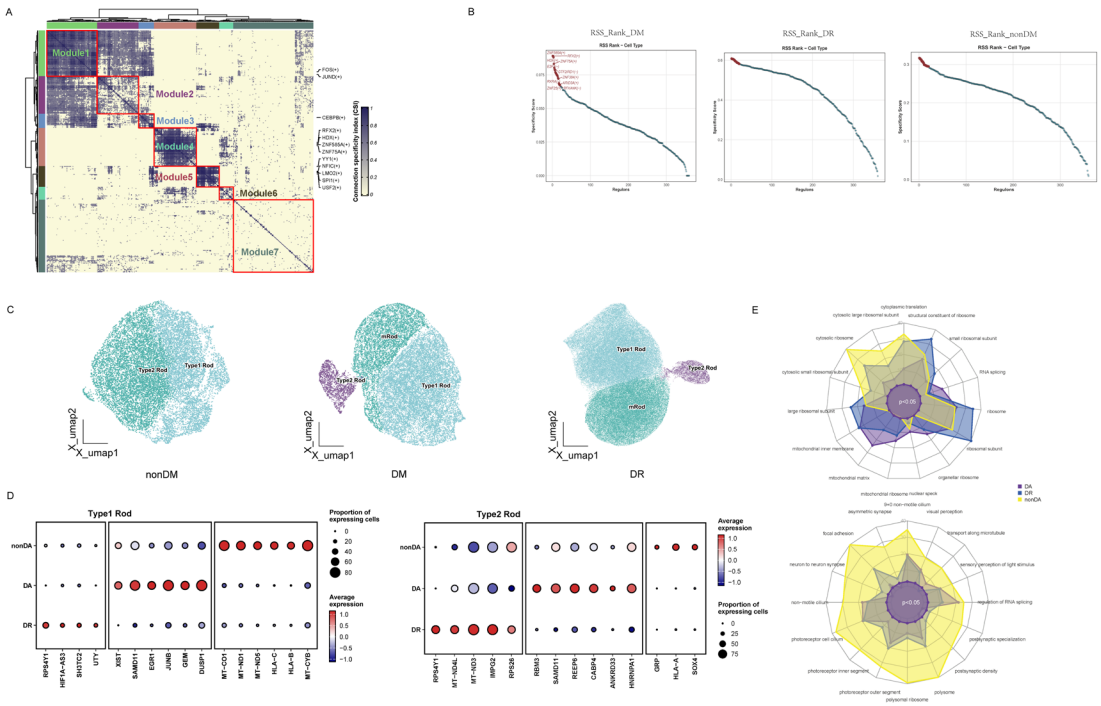

Fig8 Gene regulatory networks in retinal microglia and characterization of rod subtypes and their transcriptional dynamics during DR progression.

(A) Correlation heatmap showing seven distinct transcriptional modules (Module 1-7) identified through SCENIC analysis and CSI module detection.

(B) RSS ranking analysis showing the distribution of TF activities across disease conditions (nonDM, DM, DR). Each plot displays the ranked transcription factors based on their regulatory strength specific to each condition.

(C) UMAP visualization of rod photoreceptor populations across disease conditions (nonDM, DM, DR), showing Type1 Rod and Type2 Rod distributions. Each panel represents a different condition, demonstrating the emergence of distinct rod subtypes.

(D) Dot plots showing expression patterns of differential expressed genes in Type1 Rod and Type2 Rod populations across disease conditions (nonDM, DM, DR). Dot size represents the proportion of expressing cells, and color intensity indicates average expression level.

836 (E) Radar plots showing GO enrichment analysis across disease conditions with DM (purple), DR (blue),

837 and nonDM (yellow).

838

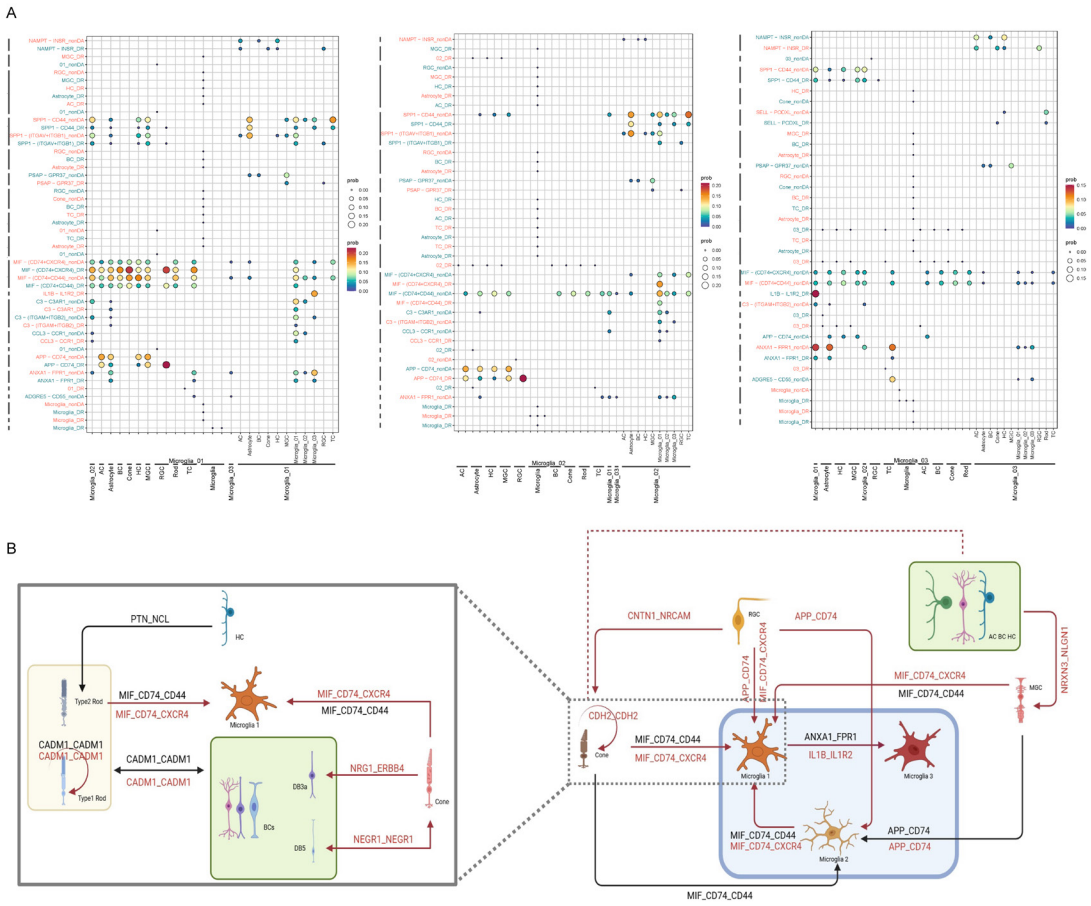

Fig9 Cell-cell communication analysis of human retina.

(A) Cell-cell communication analysis showing four key signaling pathways (ANXA1-FPR1, IL1B-IL1R2, MIF-CD74-CXCR4, and APP-CD74) between microglial subtypes and other retinal cells across disease conditions.

(B) Dynamic remodeling of neural-immune cell communication networks in the human retina during DR progression. This figure was created using BioRender.

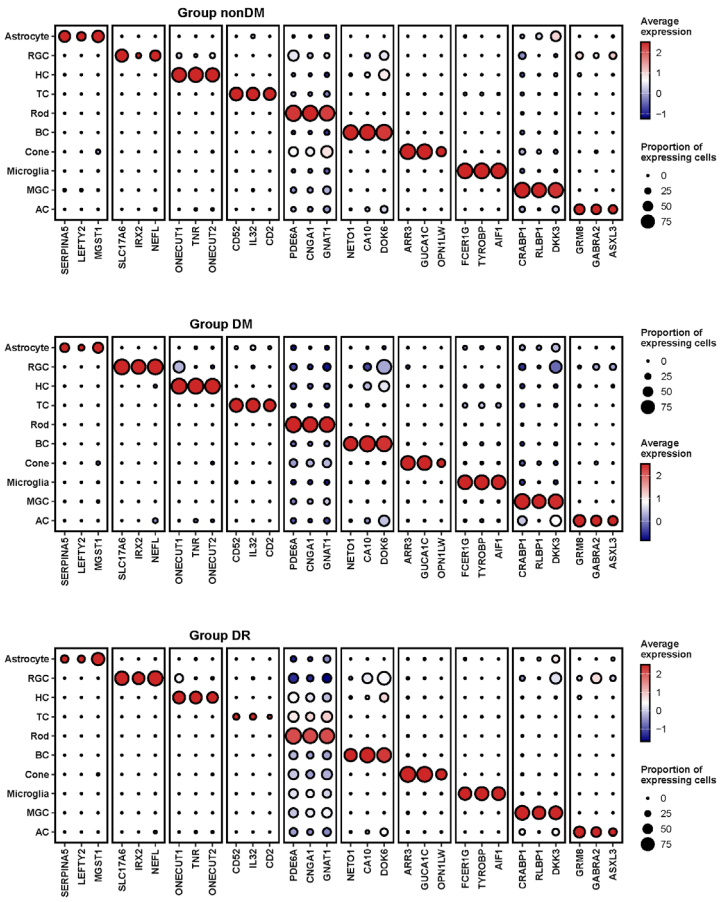

FigS1 Gene expression patterns across retinal cell types in nonDM, DM, and DR conditions separately. Dot plots showing the expression of key genes across major retinal cell types, including astrocytes, RGCs (retinal ganglion cells), HCs (horizontal cells), rods, BCs (bipolar cells), cones, microglia, MGCs (Müller glia cells), and ACs (amacrine cells). Each panel represents a specific condition: nonDM (top), DM (middle), and DR (bottom). Dot size represents the proportion of expressing cells within each cell type, while color intensity indicates the average expression level.

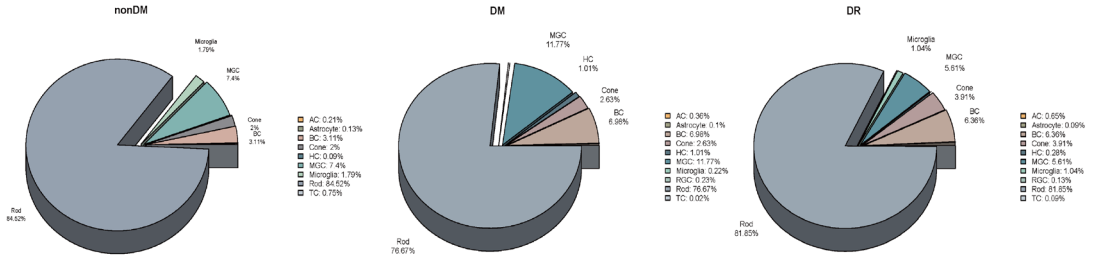

FigS2 Cellular composition across retinal cell types in nonDM, DM, and DR conditions. Pie charts showing the proportion of major retinal cell types, including rods, cones, bipolar cells (BC), horizontal cells (HC), amacrine cells (AC), Müller glia cells (MGC), microglia, astrocytes, T cells (TC), and retinal ganglion cells (RGC).

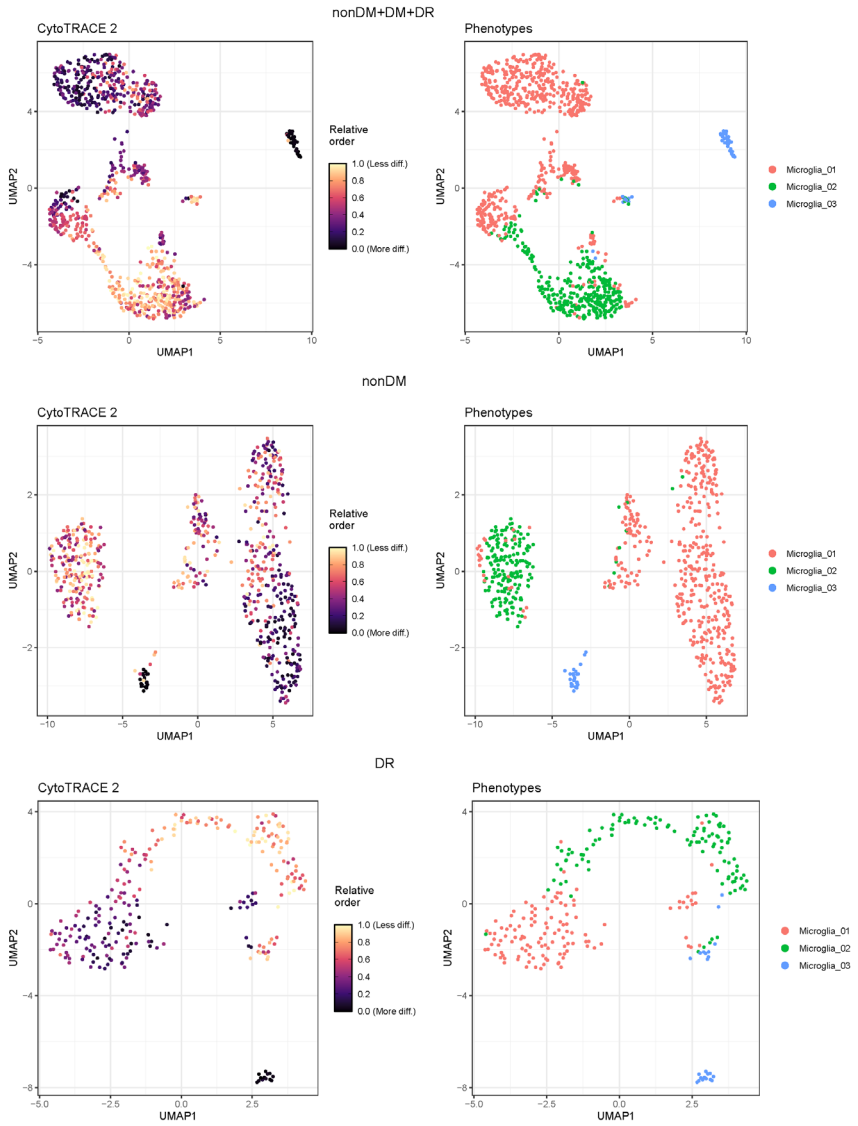

FigS3 CytoTRACE2 analysis of microglial population of human retina across different conditions. UMAP visualizations of microglial populations are shown, colored by CytoTRACE2 differentiation scores (left) and microglial subtypes (right) across integrated (nonDM+DM+DR), nonDM, and DR datasets. CytoTRACE2 scores range from less differentiated (yellow) to more differentiated (purple). Microglial subtypes are labeled as Microglia_1 (red), Microglia_2 (green), and Microglia_3 (blue).

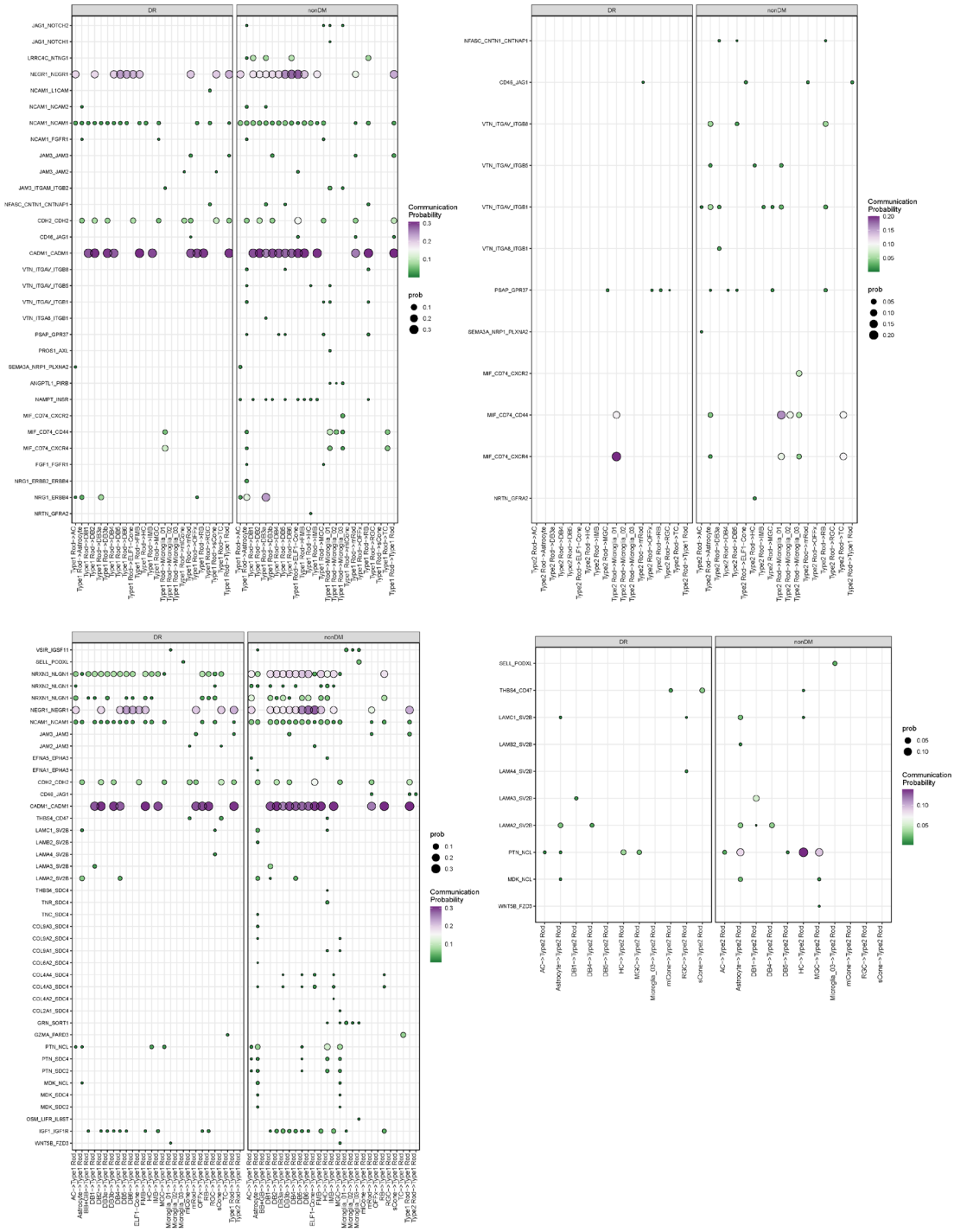

FigS4 Cell-cell communication analysis of nonDM and DR conditions, focusing on Type1 Rod and Type2 Rod as senders and receivers. Dot plots showing ligand-receptor interactions between retinal cell types, including photoreceptors (Type1 Rod, Type2 Rod, Cone), bipolar cells (BCs), horizontal cells (HCs), retinal ganglion cells (RGCs), Müller glia cells (MGCs), and microglial subtypes (Microglia_1,

873 Microglia_2, Microglia_3). Dot size represents the strength of communication (interaction score), and

874 color intensity indicates the communication probability.

875

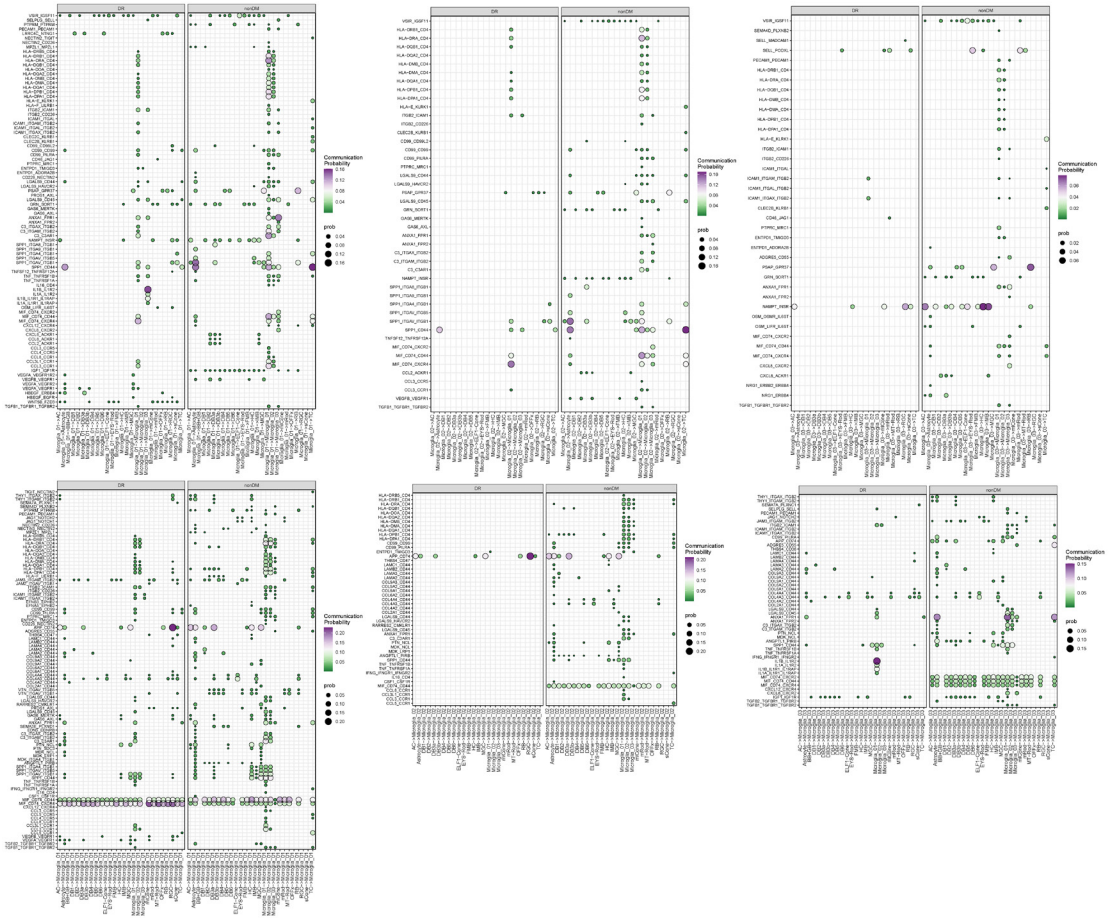

FigS5 Cell-cell communication analysis in nonDM and DR conditions, highlighting Microglia_1, Microglia_2, and Microglia_3 as both senders and receivers. Dot plots display ligand-receptor interactions between retinal cell types, including photoreceptors (Type1 Rod, Type2 Rod, Cone), bipolar cells (BCs), horizontal cells (HCs), retinal ganglion cells (RGCs), Müller glia cells (MGCs), and microglial subtypes. Dot size represents interaction strength (communication score), while color intensity indicates communication probability.

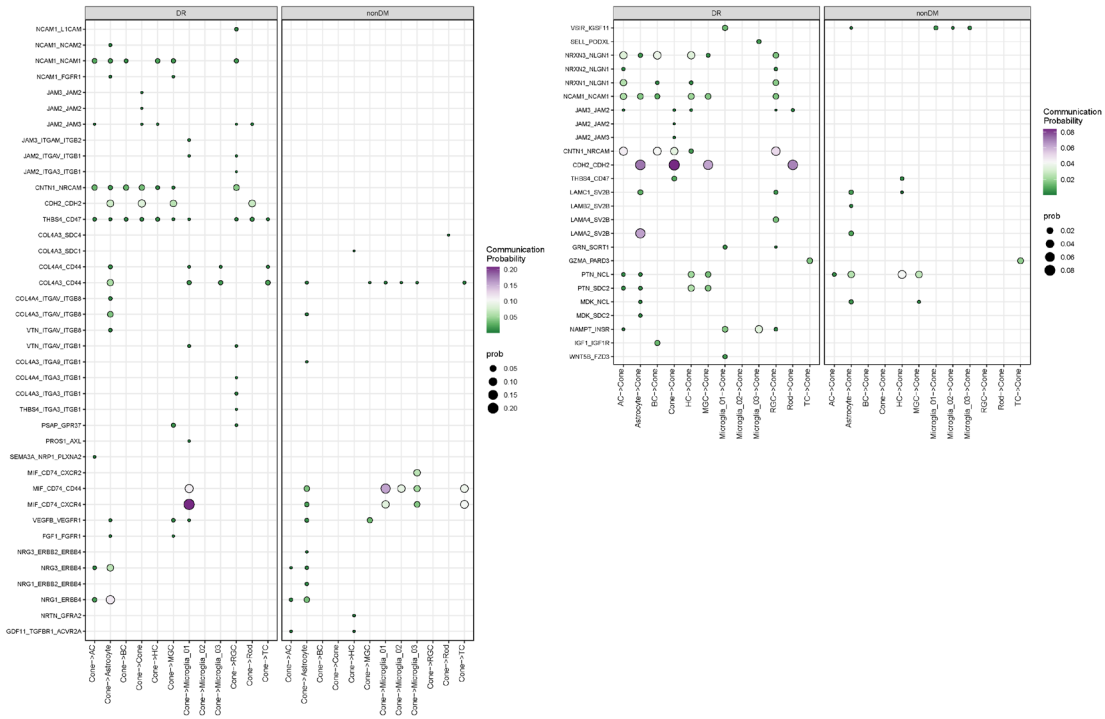

FigS6 Cell-cell communication analysis of nonDM and DR conditions, focusing on cones as senders and receivers. Dot plots showing ligand-receptor interactions between cones and other retinal cell types, including Type1 Rod, Type2 Rod, bipolar cells (BCs), horizontal cells (HCs), retinal ganglion cells (RGCs), Müller glia cells (MGCs), and microglial subtypes (Microglia_1, Microglia_2, Microglia_3). Dot size represents the strength of communication (interaction score), and color intensity indicates the communication probability.

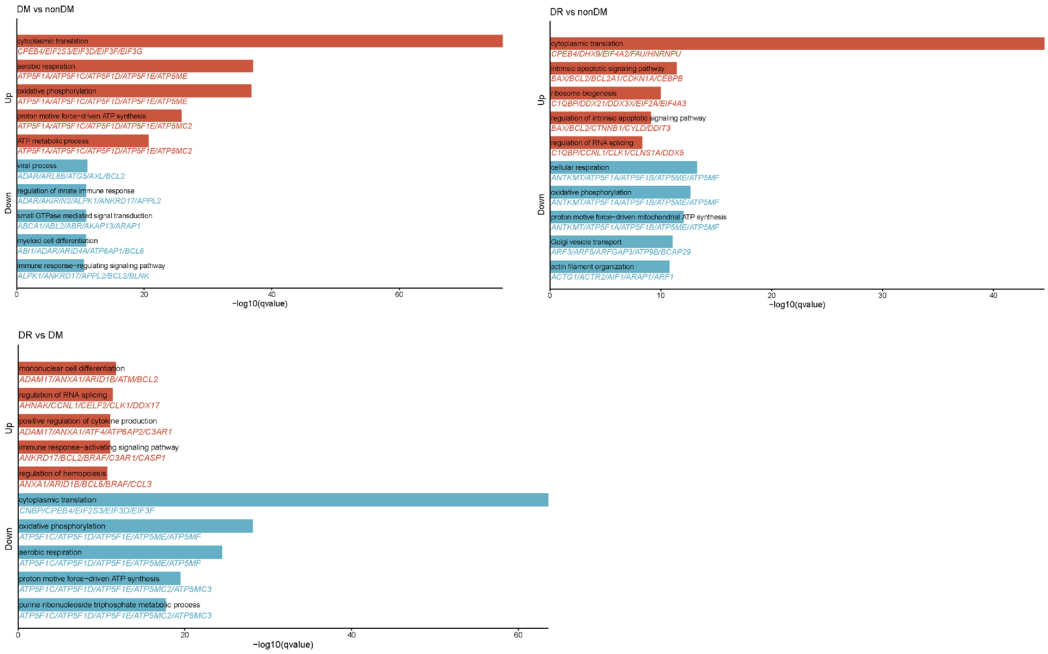

FigS7 GO enrichment analysis showing significantly enriched biological processes across DR progression. Bar plots display GO terms for upregulated (red) and downregulated (blue) genes in pairwise comparisons: DM vs nonDM (top left), DR vs nonDM (top right), and DR vs DM (bottom). The x-axis represents -log10(qvalue), indicating the significance of enrichment, while the y-axis lists the GO terms.

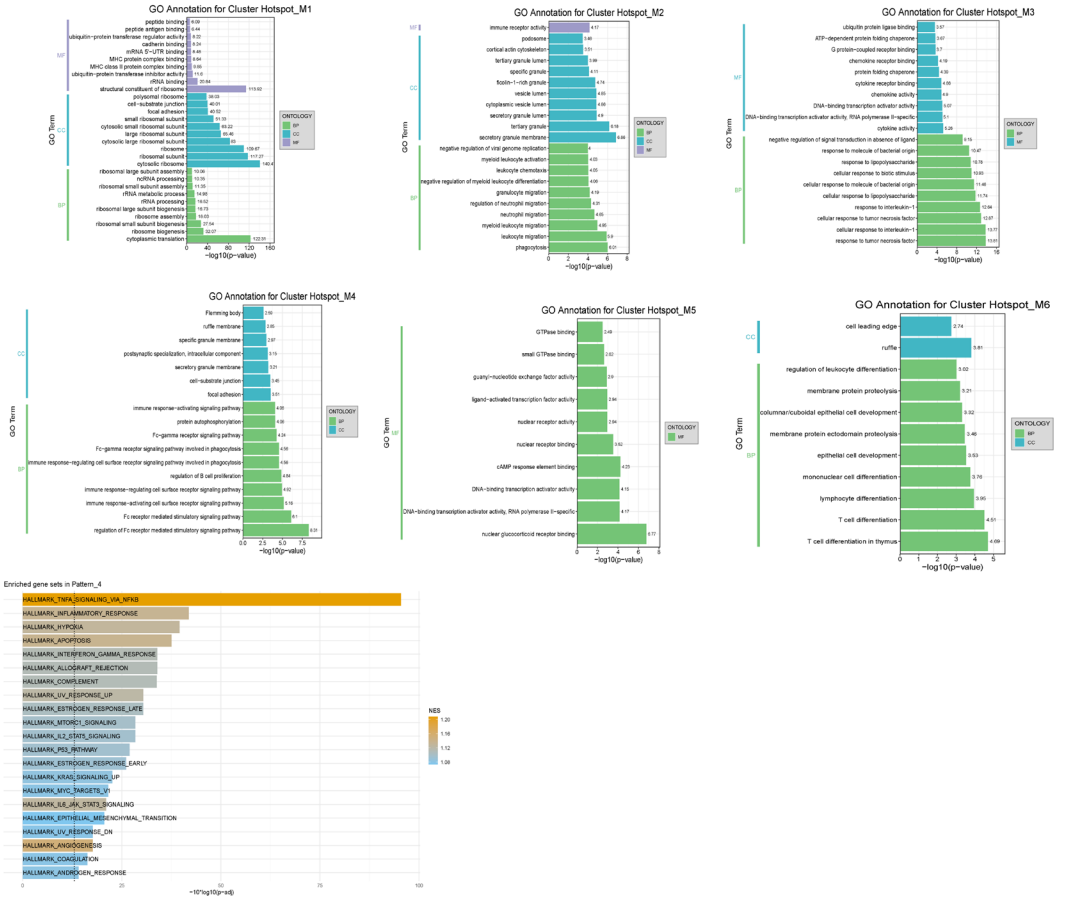

FigS8 GO enrichment of transcriptional modules identified in microglia. The top two rows display GO enrichment analysis for Hotspot modules (Hotspot_M1 to Hotspot_M6). Bar plots show significantly enriched GO terms, with bar length representing -log10(pvalue). GO terms are categorized into three categories: biological process (BP), cellular component (CC), and molecular function (MF). The bottom panel shows enriched hallmark gene sets in Pattern_4 identified through pathway analysis of CoGAPS results. Bar length represents -log10(adjusted p-value), and color intensity indicates normalized enrichment scores (NES).

TableS1 Donor information and retinal cell composition of thirteen samples in this study. This table provides detailed information about the donors, including donor ID, other disease status, eye condition, sex, age, diabetic status, and reason for eye removal or death. Additionally, it includes the proportions and counts of major retinal cell types (astrocytes, bipolar cells, cones, horizontal cells, Müller glia cells, microglia, retinal ganglion cells, rods, amacrine cells, and T cells) for each retina sample.

TableS2 Gene lists of Hotspot modules, hdWGCNA modules, and CoGAPS modules identified in microglia.

TableS3 TF module assignments identified through CSI analysis.

TableS4 Differentially expressed genes between Type1 Rod and Type2 Rod.

TableS5 Differentially expressed genes between disease conditions (DR vs DM vs nonDM) in Type1 Rod.

TableS6 Differentially expressed genes between disease conditions (DR vs DM vs nonDM) in Type2 Rod.

TableS7 Differentially expressed genes between microglial subtypes.

TableS8 Differentially expressed genes between disease conditions (DR vs DM vs nonDM).

TableS9 Differentially expressed genes between disease conditions (DR vs DM vs nonDM).

TableS10 Differentially expressed genes between disease conditions (DR vs DM vs nonDM) in cone.